

UNIVERSITY OF PADOVA

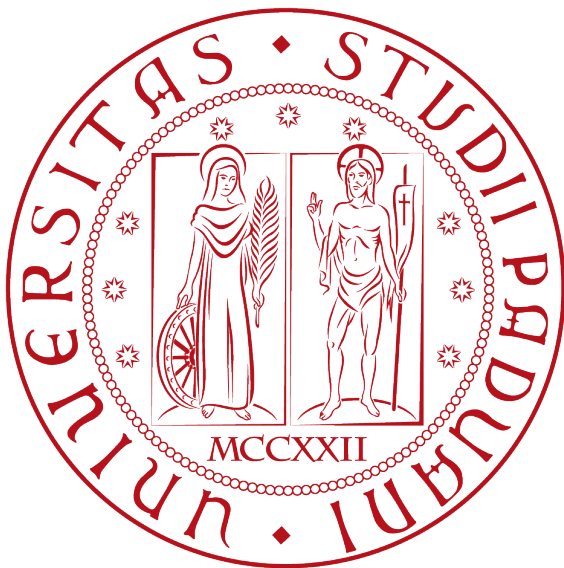
---

EXERCISES  
of  
NUMERICAL METHODS  
in  
SOFT MATTER

---

Created By

RICCARDO TANCREDI



All the codes related to the outputs shown here can be found on my [Github page](#).

# 1 Sampling

## 1.1 Exercise: Sampling random points within D-dimensional domains by hit and miss

**Rectangle** I have generated  $N = 10^6$  random points in the rectangle  $[0.2, 0.8] \times [0.7, 0.9]$ . Theoretically the area is given by  $A = (b - a) \cdot (d - c) = 1.2 \cdot 10^{-1}$ . Using the MonteCarlo hit-miss method the estimated area is

$$A^{MC} \simeq 1.197 \cdot 10^{-1}.$$

**Disk** In the same manner, for a disk of radius  $R = 1$ , the area is of course  $A_d = \pi R^2 = 3.141593\dots$ . Sampling points via MonteCarlo such that  $\sqrt{x^2 + y^2} \leq R$  is

$$A_d^{MC} = 3.142520\dots$$

## Sampling random numbers from a given distribution

### 1.2 Exercise: Inversion method

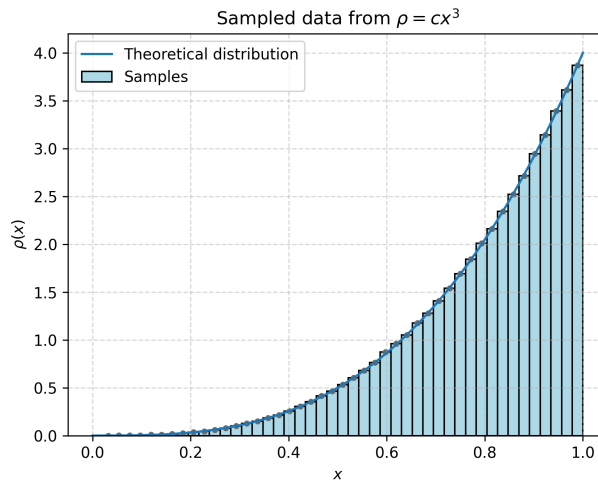
The normalization constant is  $c = n + 1$ : in this way  $\int_0^1 \rho(x) = 1$ . Setting then  $n = 3$ , the CDF of  $\rho(x)$  is

$$P(x) = x^{n+1}$$

The inversion method allows us to sample from  $\rho(x)$  by choosing

$$x = (u)^{\frac{1}{n+1}}$$

where  $u$  is a random number in  $[0, 1]$ . The result is here shown:



### 1.3 Exercise: Inversion method II

Integrating  $\rho(x) = cx^2$  for  $x \in [0, 2]$ , one gets  $c = 3/8 = 0.375$ .

Using MonteCarlo, I have integrated  $\rho(x)$  and found  $c_{MC} = 0.3745262$ , in agreement with the theoretical result.

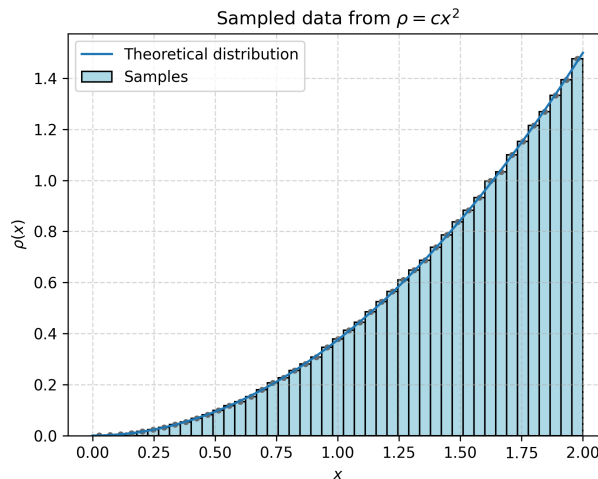
As before, the CDF of  $\rho(x)$  is

$$P(x) = \frac{c}{3}x^3$$

which allows us to sample  $x$  by inversion:

$$x = \sqrt[3]{3u/c};$$

where  $u$  is a random number in  $[0, 1]$ . The values sampled from  $\rho(x)$  are here presented:



## 1.4 Additional exercises

1.

Starting from  $\rho(x) = \mu e^{\mu x}$  for  $x \geq 0$ , the cumulative distribution is given integrating:

$$P(x) = \int_0^x \mu e^{\mu x'} dx' = 1 - e^{-\mu x}$$

Sampling a number  $u$  in the  $[0, 1]$  interval and inverting the last equation, one gets to

$$1 - e^{-\mu x} = u \iff x = -\frac{\log(1 - u)}{\mu}$$

The values sampled from  $\rho(x)$  are here presented:

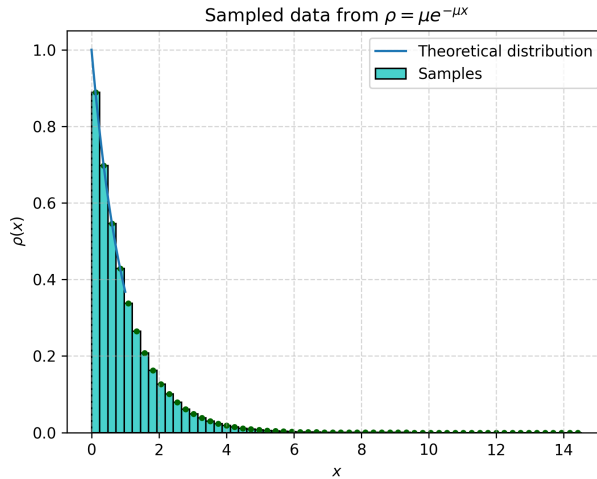


Figure 1.1: Inversion method for  $\rho(x)$  with  $\mu = 1$

2.

Starting from  $\rho(x) = 2xe^{-x^2}$  for  $x \geq 0$ , the integral function is

$$P(x) = \int_0^x 2x'e^{-x'^2} dx' = 1 - e^{-x^2}$$

Finally,

$$1 - e^{-x^2} = u \iff x = \sqrt{-\log(1 - u)}$$

where  $u \in [0, 1]$ . The values sampled from  $\rho(x)$  are here presented:

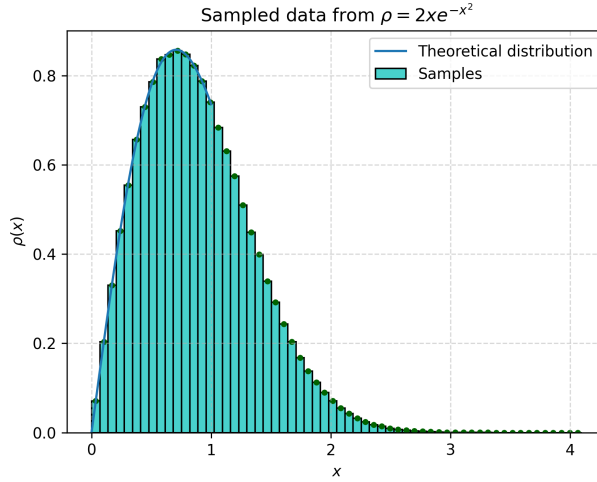


Figure 1.2: Inversion method for  $\rho(x)$

### 3.

From  $\rho(x) = \frac{1}{(a+bx)^n}$  for  $x \geq 0$  and  $n > 1$ , the cumulative function is

$$P(x) = \int_0^x \frac{1}{(a+bx')^n} dx' = \frac{(a+bx)^{1-n}}{b(1-n)} - \frac{a^{1-n}}{b(1-n)}$$

Since  $\int_0^{+\infty} \rho(x) dx \stackrel{!}{=} 1$  one gets the normalization condition that  $a$  and  $b$  must satisfy:

$$b = -\frac{a^{1-n}}{1-n}$$

Then,  $x$  is calculated easily by the inversion method, sampling a random number  $u \in [0, 1]$ :

$$P(x) = u \iff x = \frac{\left[ \left( u + \frac{a^{1-n}}{b(1-n)} \right) \cdot b(1-n) \right]^{\frac{1}{1-n}} - a}{b}$$

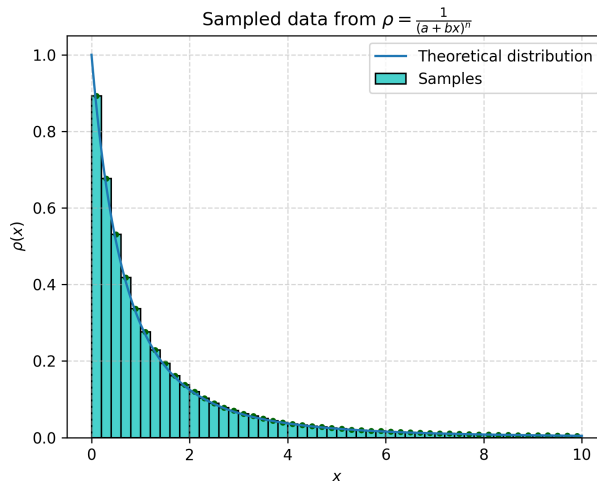


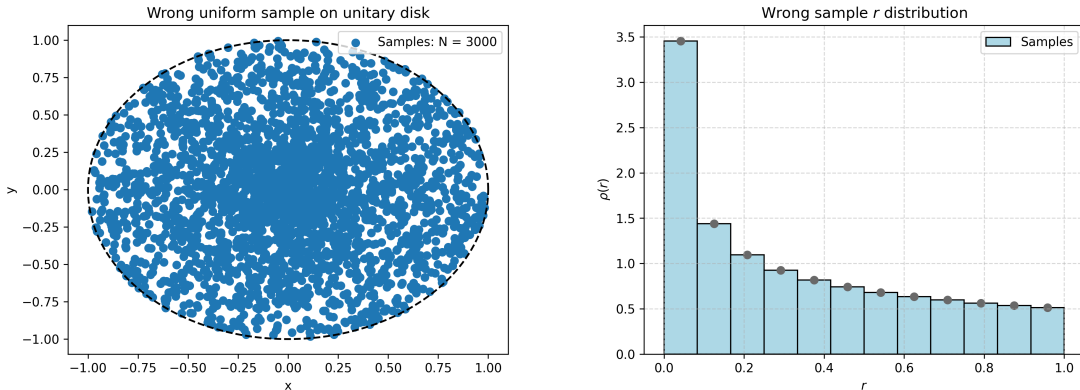
Figure 1.3: Inversion method for  $\rho(x)$ ,  $a = 1$ ,  $b = 0.5$  and  $n = 3$

# 2 Sampling via transformation of coordinates

## 2.1 Exercise: Sampling uniformly points within a unit radius disk

In the plot below, the data plotted are sampled according to  $r = u$ ,  $\theta = 2\pi u'$ , where  $u, u' \in [0, 1]$ . It is possible to see that points are not uniformly distributed on a circle, as highlighted by the higher concentration of points around the center (right plot).

The conceptual mistake of this algorithm is to not have considered the dependence of  $r$  and  $\theta$ . In cartesian coordinates we can use this method to generate  $x = r \cdot \cos(\theta)$  and  $y = r \cdot \sin(\theta)$ , but  $\theta = \tan^{-1}(y/x)$  depends on both  $x$  and  $y$  as  $r = \sqrt{x^2 + y^2}$  and it is not fully independent.



In order to fix this, we correctly apply the change of variables:

$$p(r, \theta) = p(x, y) \cdot r = \frac{r}{\pi R^2}$$

and  $p(r) = \int p(r, \theta) d\theta = \frac{2r}{R^2}$ , where  $r \in [0, R]$ .

Finally:

$$p(\theta|r) = p(r, \theta)/p(r) = \frac{1}{2\pi}$$

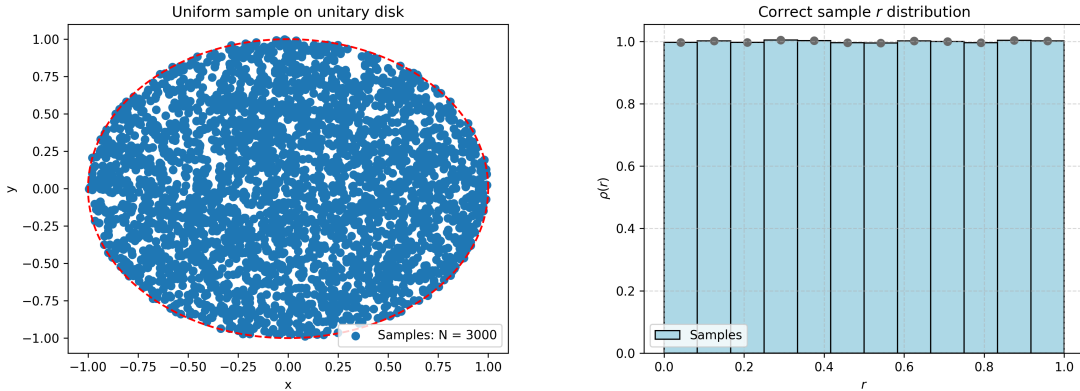
In order to sample from  $p(r)$ , the cumulative  $P(r)$  is given by:

$$P(r) = \int_0^r p(r') dr' = (r/R)^2 = u \iff r = \sqrt{u \cdot R^2}$$

Instead, the cumulative of  $p(\theta|r)$  is:

$$P(\theta|r) = \int_0^\theta p(\theta'|r) d\theta' = \theta/(2\pi) = u' \iff \theta = 2\pi u'$$

where  $u, u' \in [0, 1]$ .



As before, the left plot shows  $10^3$  generated points, highlighting now visually the correct distribution. On the right it is possible to see the distribution of all the points ( $10^6$  total samples) as a function of the distance  $r$ . The picture above shows clearly a uniform sampling, while the one before presented points out an higher concentration near the center of the circle.

## 2.2 Exercise: Box-Muller transformation

By using the above results, we sample  $r \sim p(r)$  and  $\theta \sim p(\theta)$  by inverting the relations shown in class:

$$p(r, \theta)drd\theta = 1/(2\pi)\exp(-r^2/2)drd\theta = p(r)p(\theta)drd\theta$$

Therefore, it is possible to sample  $r \sim p(r)$  and  $\theta \sim p(\theta)$ .

In order to draw  $r \sim p(r)$ , the cumulative  $P(r)$  is given by:

$$\begin{aligned} P(r) &= \int_0^r r' \exp(-r'^2/2) dr' \\ &= 1 - \exp(-r^2/2) \end{aligned}$$

and setting  $P(r) = u \iff r = \sqrt{-2 \log(1-u)}$ .

To draw  $\theta \sim p(\theta)$ , the cumulative  $P(\theta)$  is of course:

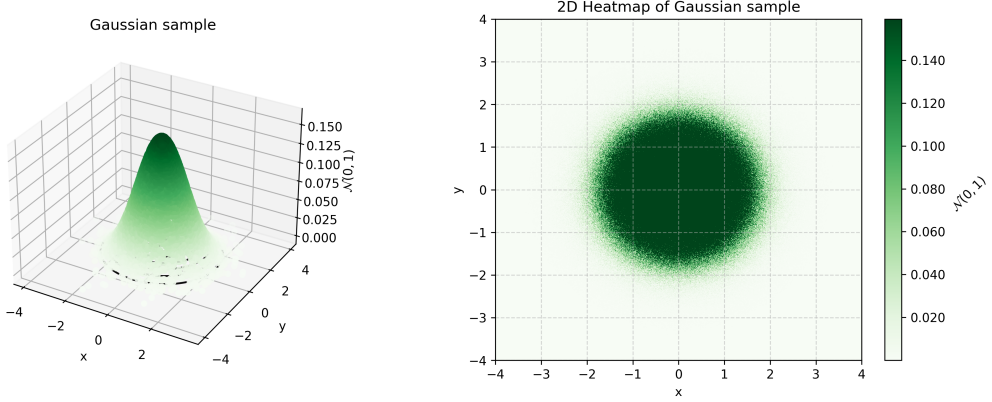
$$\begin{aligned} P(\theta) &= \int_0^\theta d\theta'/(2\pi) \\ &= \theta/(2\pi) \end{aligned}$$

Setting  $P(\theta) = u' \iff \theta = 2\pi u'$ , with  $u, u' \in [0, 1]$ . Finally we can summarize the results in

$$\begin{cases} r = \sqrt{-2 \log(1-u)} \\ \theta = 2\pi u' \end{cases}$$

where  $u, u' \in [0, 1]$ .

What we get is a normal distribution.



The above can be easily extended to the most general case of  $\mathcal{N}(\mu, \sigma^2)$ : starting from  $p(r, \theta)$ , the new samples  $x' = \sigma x + \mu = \sigma r \cos(\theta) + \mu$  and  $y' = \sigma r \sin(\theta) + \mu$ , where  $r, \theta \sim p(r, \theta)$ . Therefore, sampling from  $\mathcal{N}(0, 1)$  allows us to get any Gaussian of mean  $\mu$  and variance  $\sigma^2$ .

### 2.3 Exercise: Rejection method

In order to be normalized, the  $g(x)$  function has constant value  $A = 2p/(2p^2 + 1)$ .

The  $c$  constant can have multiple possible values. For  $x \in [0, p]$ , to achieve  $f(x) \leq c \cdot g(x)$ , I have set

$$c \geq \frac{\sqrt{2/\pi}}{A}.$$

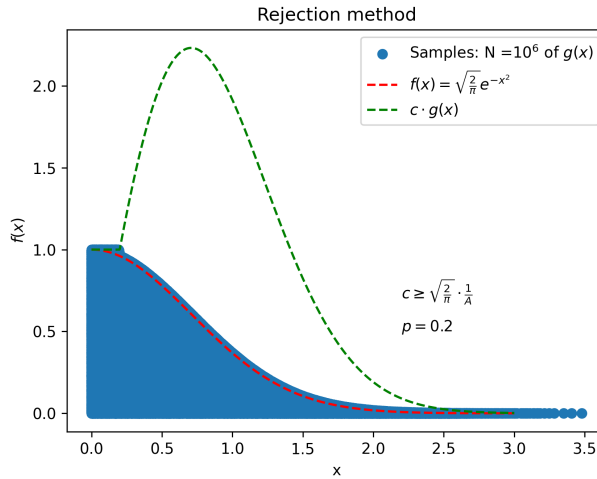
The cumulative of  $g(x)$  is the function

$$G(x) = \begin{cases} Ax & \text{for } 0 \leq x \leq p \\ 1 - A/(2p) \cdot e^{-(p^2 - x^2)} & \text{for } x > p \end{cases}$$

Applying the inverse method to generate a sample  $X$  from  $g(x)$  one gets:

$$x = \begin{cases} u/A & \text{for } 0 \leq u \leq pA \\ x = \sqrt{p^2 - \log(2(1-u) \cdot p/A)} & \text{for } u > pA \end{cases}$$

The results are here presented, having sampled  $N = 10^6$  points for  $p = 0.2$ .



Furthermore, here below it is presented the efficiency of the performance of the method by varying  $p$ . It is defined as the number of accepted points over  $N = 10^6$  total attempts.

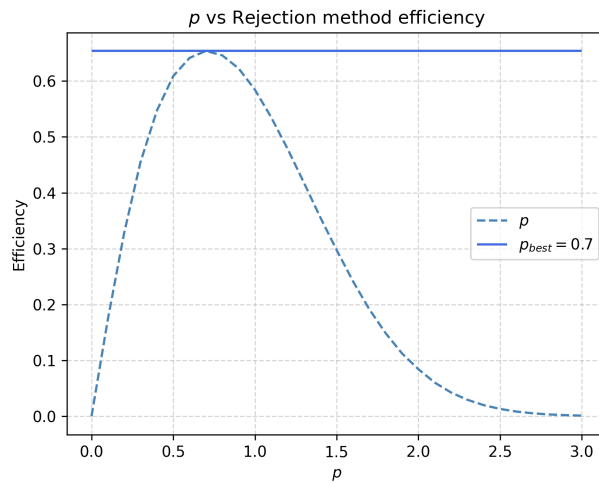


Figure 2.4: The best efficency is found for  $p = 0.7$

# 3 Importance sampling

## 3.1 Exercise

The integral estimated via a crude approach is

$$I_{crude} = 0.2142484$$

with  $g(x) = \frac{x^2}{x^2+1}$  chosen as slowly varying function. This result is not far from the theoretical value

$$I_{th} = 0.2145802.$$

A better result can be achieved using instead the importance sampling method, generating a sample  $X$  from the function  $W(x)$ .  $W(x)$  is the  $f(x)$  function from which we have sampled in the previous exercise: since now the requirement is that  $W(x)$  is a PDF, it must be normalized in the  $[0, +\infty]$  interval. So  $W(x) \rightarrow A \cdot W(x)$  where  $A = \sqrt{2}$ .

This means that after evaluating  $g(x_i)$  and summing for  $i$  going from 0 to  $N = 10^6$ , we have to multiply not only for  $\sqrt{\pi/2}$  but also for  $1/A$ , so for  $\sqrt{\pi/2} = \sqrt{\pi/4}$ .

The result now obtained is

$$I_{I.S.} = 0.2144030$$

in better agreement with  $I_{th}$ .

## 3.2 Exercise

In this last exercise the goal is to apply the same method as before, but with  $f(x) = \cos(x)$  and  $g(x) = a + bx^2$ , which has cumulative

$$G(x) = ax + \frac{b}{3}x^3$$

for  $x \in [0, \pi/2]$ . First thing to do is to invert a cubic formula. The algorithm capable of finding the inverse of a cubic equation has been implemented in C using the Cardano relations.

The way  $a, b$  had been chosen is given by the requirement that  $h(x) = f(x)/g(x) \sim const.$  and the constraint that  $g(x)$  in  $[0, \pi/2]$  must be normalized.

Therefore,  $a$  and  $b$  are linked and they must approximate the  $f(x) = \cos(x)$  for  $x \in [0, \pi/2]$ . This is achieved by requiring that  $g(0) = f(0) = 1 \rightarrow a = 1$  and  $g(\pi/2) = f(\pi/2) = 0 \rightarrow b = -\frac{4}{\pi^2}$ .

Of course, given  $b$ ,  $a \sim 1$  since the normalization constraint must be satisfied. Then, the sum over  $h(x_i)$  ( $i \in [1, k]$ , where  $k \rightarrow N$ ) is performed and the final integral is given by dividing by  $k$ , which represents the number of iterations  $1 \leq k \leq N$  in order to have an accuracy  $\sim 1\%$ .

$$\boxed{\text{From the normalization constraint: } a = \left(1 - \frac{b\pi^3}{24}\right) \cdot \frac{2}{\pi}}$$

Theoretically the integral is

$$\int_0^{\pi/2} \cos(x) dx = 1$$

and the estimate via importance sampling is

$$I_{k=4}^{acc \sim 1\%} = 0.9956183$$

with an accuracy of  $\sim 4 \cdot 10^{-3}$  after just 4 iterations.

### 3.3 Exercise

Starting from

$$\begin{aligned} \langle f \rangle_p &= \int_{\mathbb{R}} f(x) \rho(x) dx \\ &= \int_{\mathbb{R}} f(x) \frac{\rho(x)}{g(x)} g(x) dx \\ &= \int_{\mathbb{R}} f(x) \frac{\rho(x)}{g(x)} dg \\ &= \langle f \cdot \frac{\rho}{g} \rangle_g \\ &=: \langle F \rangle_g \end{aligned}$$

First, it is possible to show that

$$\begin{aligned} \langle f \rangle_p &= \int_{\mathbb{R}} f(x) \rho(x) dx \\ &= \int_{-\infty}^T 0 \cdot \rho(x) dx + \int_T^{+\infty} 1 \cdot \rho(x) dx \\ &= \int_T^{+\infty} e^{-x} dx = -e^{-x} \Big|_T^{+\infty} \\ &= e^{-T} \end{aligned}$$

And in the same way,

$$\begin{aligned} \sigma^2(f) &= \langle f^2 \rangle_p - (\langle f \rangle_p)^2 \\ &= \int_{\mathbb{R}} f(x)^2 \rho(x) dx - (\langle f \rangle_p)^2 \\ &= \int_{-\infty}^T 0 \cdot \rho(x) dx + \int_T^{+\infty} 1^2 \cdot \rho(x) dx - (\langle f \rangle_p)^2 \\ &= \int_T^{+\infty} e^{-x} dx - (\langle f \rangle_p)^2 = e^{-T} - e^{-2T} \\ &= \langle f \rangle_p \left(1 - \langle f \rangle_p\right) \end{aligned}$$

Finally:

$$\begin{aligned}
\sigma^2(a, f(x)\rho(x)/g(a,x)) &= \sigma^2(a, F(x)) \\
&= \int_{\mathbb{R}} F(x)^2 g(x) dx - (\langle F \rangle_g)^2 \\
&= \int_T^{+\infty} \frac{\rho(x)^2}{g(x)} dx - \left( \int_T^{+\infty} \rho(x) dx \right)^2 \\
&= \frac{1}{a} \int_T^{+\infty} e^{-x(2-a)} dx - \left( \int_T^{+\infty} e^{-x} dx \right)^2 \\
&= \frac{1}{a} \left( -\frac{e^{-x(2-a)}}{3-2a} \Big|_T^{+\infty} \right) - \left( -e^{-x} \Big|_T^{+\infty} \right)^2 \\
&= \frac{e^{-T(2-a)}}{a(2-a)} - e^{-2T}
\end{aligned}$$

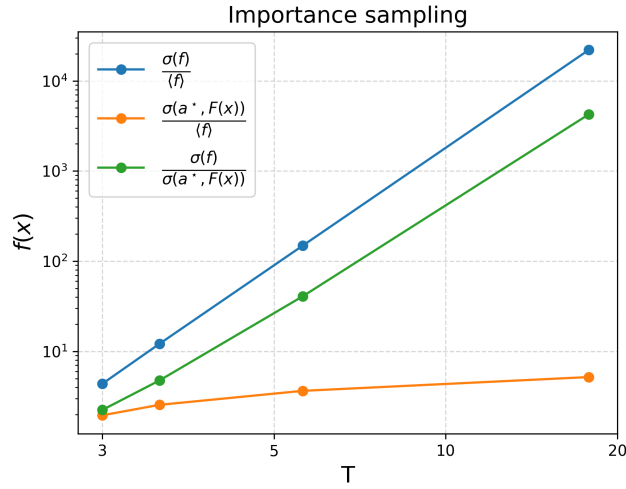
The value  $a^*$  at which  $\sigma^2(a, F(x))$  is minimum is given by differentiating:

$$\frac{\partial \sigma^2(a, F(x))}{\partial a} = e^{-T(2-a)} \frac{aT(2-a) - (2-2a)}{a^2(2-a)^2} \stackrel{!}{=} 0 \implies Ta^2 - 2a(1+T) + 2 = 0 \iff a_{1/2} = \frac{(T+1) \pm \sqrt{T^2+1}}{T}$$

Since  $0 < a \leq 1$  we have that the variance is minimized when  $\boxed{a^* = \frac{(T+1) - \sqrt{T^2+1}}{T}}.$

If we compare the values as suggested:

$$\begin{cases} \frac{\sigma^2(f)}{\langle f \rangle} = \cancel{\frac{\langle f \rangle(1-\langle f \rangle)}{\cancel{\langle f \rangle}}} = 1 - e^{-T} \\ \frac{\sigma(f)}{\sigma(a^*, F(x))} = g(T) \end{cases}$$



The plot shows the improvement in the statistical errors at different  $T$ . As expected, the ratio  $\frac{\sigma(a^*, F(x))}{\langle f \rangle}$  outperforms the previous  $\frac{\sigma(f)}{\langle f \rangle}$  ratio, witnessing the importance sampling method for larger and larger  $T$ .

# 4 Markov Chains

## 4.1 Esercise

$$\begin{aligned}
 \mu_n(i) &= \sum_j \mu_{n-1}(j)p_{ij} \\
 &= p_{ii}\mu_{n-1} + \sum_{j \neq i} p_{ij}\mu_{n-1}(j) \\
 &\stackrel{(a)}{=} \left(1 - \sum_{j \neq i} p_{ij}\right)\mu_{n-1}(i) + \sum_j \mu_{n-1}(j)p_{ij}
 \end{aligned}$$

where in (a) the property of the Stochastic matrix has been used:

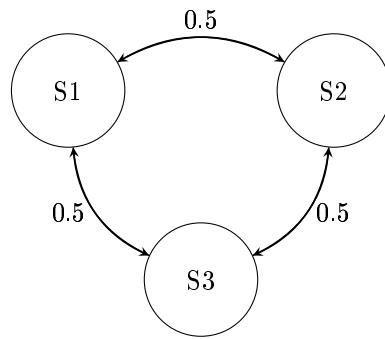
$$1 = \sum_j p_{ij} = \sum_{j \neq i} p_{ij} + p_{ii} \iff p_{ii} = 1 - \sum_{j \neq i} p_{ij}.$$

This equation tells us that a generic entry  $i$  of the state probability vector  $\vec{\mu}$  depends on two terms: the first one resembles the transition probability of leaving the site  $i$  (outflow probability), while the second term represents the transition to  $i$  from a generic state  $j$ , weighted properly by the  $p_{ij}$  element of the stochastic matrix  $\mathcal{P}$  (inflow probability).

In other words, the one found is nothing else that a master equation for  $\mu_n(i)$ .

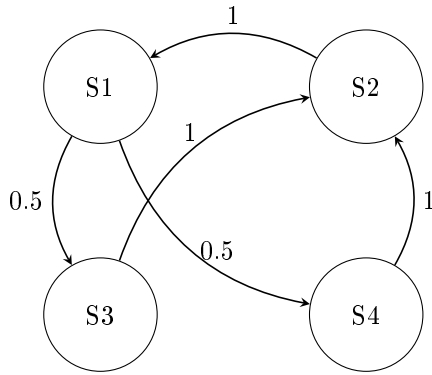
## 4.2 Exercise: digraph

(A)



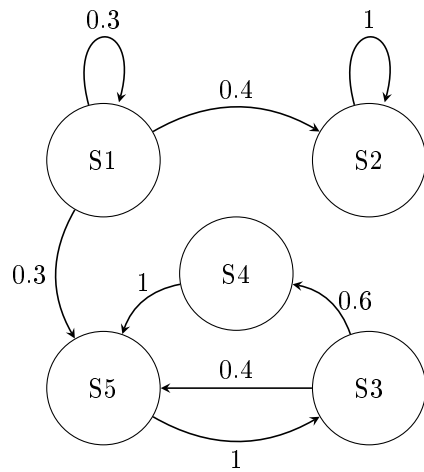
It is easy to see that each state communicates with the others, so it is accessible from all the others. The Markov Chain is therefore irreducible. Moreover, it is also recurrent.

(B)



The graph highlights the accessibility of each state. Moreover, the Markov Chain is recurrent.

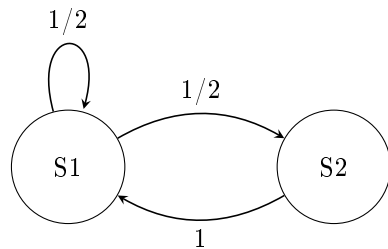
(C)



Conversely, this Markov Chain is not irreducible:  $S_2$  state communicates only with itself, so there is not a path for each pair of states. At the same time, this Markov Chain is not recurrent too: if we start from  $S_4$  for example, the probability of reaching  $S_1$  or  $S_2$  in a finite time is 0, since it is impossible to reach these states. All states  $S_1$ ,  $S_2$ ,  $S_3$ ,  $S_4$ , and  $S_5$  are recurrent states.

### 4.3 Exercise: irreducible

$\mathcal{P}_1$

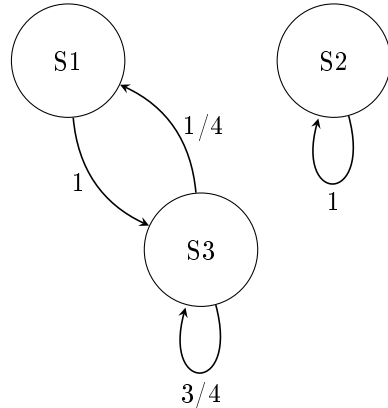


From the illustration it is possible to see that the Markov Chain is irreducible since there exists a path that connects  $S_1$  to  $S_2$  and viceversa. Since it is a finite Markov Chain and irreducible it is recurrent irreducible. The period is 1 for  $S_1$  which makes  $\mathcal{P}_1$  also aperiodic.

$$\lim_{n \rightarrow \infty} \mathcal{P}_1^n = \frac{1}{3} \begin{pmatrix} 2 & 1 \\ 2 & 1 \end{pmatrix}$$

See `exercise3.c` for the implementation and justification of this result.

$\mathcal{P}_2$

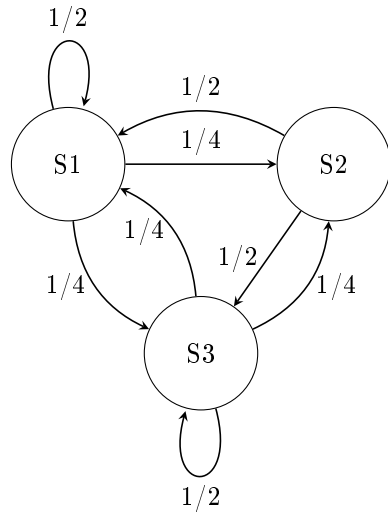


In this case instead, the Markov Chain is not irreducible since there is no state that communicates with  $S_2$ , except for  $S_2$  itself.

$$\lim_{n \rightarrow \infty} \mathcal{P}_2^n = \frac{1}{5} \begin{pmatrix} 1 & 0 & 4 \\ 0 & 1 & 0 \\ 1 & 0 & 4 \end{pmatrix}$$

See `exercise3.c` for the implementation and justification of this result.

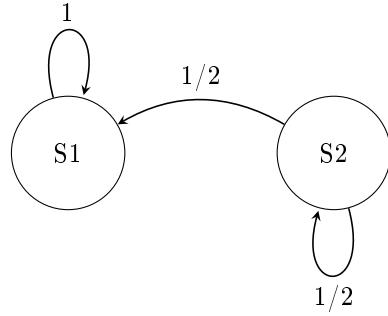
#### 4.4 Exercise: regularity



As we can see the Markov Chain is irreducible and since there exists at least an aperiodic state ( $S_1$  and  $S_3$  here) the MC is regular. Another way of to see this, is to consider  $(\mathcal{P}^2)_{jj} > 0 \forall j$ .

#### 4.5 Exercise: stationarity

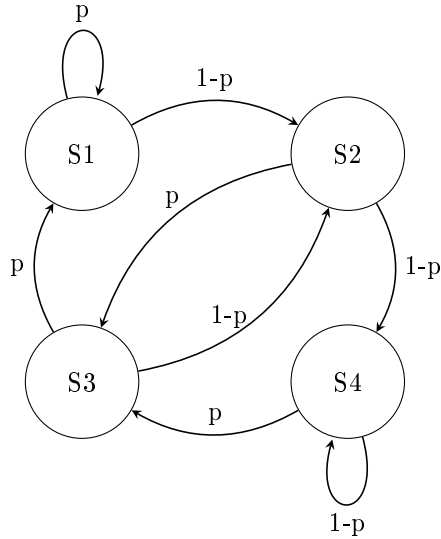
The Markov Chain defined by  $\mathcal{P} = \begin{pmatrix} 1 & 0 \\ 1/2 & 1/2 \end{pmatrix}$  can be graphed as:



It is easy to see that it is not irreducible, since  $S1$  communicates only with itself. Therefore, it is not regular.

## A

Given  $0 < p < 1$  we consider the following Markov Chain defined by the transition matrix  $\mathcal{P}$ :



It is possible to see that there exists a path between each pair of states. The MC is irreducible. Since there is a finite number of states (4) the MC is recurrent irreducible. Furthermore, there exists a state ( $S1$  and  $S4$ ) that is aperiodic, the MC is then regular. This is always true since  $p$  cannot be either 0 or 1.

In order to find the fixed point  $\pi$  we have to find the right eigenvector of  $\mathcal{P}$  with eigenvalue 0: starting from  $\pi\mathcal{P} = \pi$ , we get

$$\begin{aligned} 0 &= \pi(\mathbb{1} - \mathcal{P}) \\ &= \pi \begin{pmatrix} 1-p & p-1 & 0 & 0 \\ 0 & 1 & -p & p-1 \\ -p & p-1 & 1 & 0 \\ 0 & 0 & -p & p \end{pmatrix} \end{aligned}$$

Setting  $\pi = (a, b, c, d)$ , its entries are estimated by solving the following system of equations:

$$\begin{cases} (1-p)a = pc \\ b = (1-p)(a+c) \\ c = p(d+b) \\ pd = (1-p)b \end{cases}$$

Choosing  $a = p$ :

$$\begin{cases} a = p \\ c = 1 - p \\ b = 1 - p \\ d = \frac{(1-p)^2}{p} \end{cases} \implies \pi^* = \left( p, 1 - p, 1 - p, \frac{(1-p)^2}{p} \right)$$

Normalizing the resulting vector, such that  $\sum_i \pi_i = 1$  we get the final result:

$$\boxed{\pi = p \left( p, 1 - p, 1 - p, \frac{(1-p)^2}{p} \right)}$$

## B

As in the previous exercise:

$$\begin{aligned} 0 &= \pi(\mathbb{1} - \mathcal{P}) \\ &= \pi \begin{pmatrix} \frac{1}{2} & -\frac{1}{2} & 0 \\ -\frac{1}{4} & \frac{1}{2} & -\frac{1}{4} \\ 0 & -\frac{1}{2} & \frac{1}{2} \end{pmatrix} \end{aligned}$$

Setting  $\pi = (a, b, c)$  we have to solve the following system of equations

$$\begin{cases} 2a = b \\ a + c = b \\ b = 2c \end{cases}$$

Setting  $b = 1 \rightarrow a = \frac{1}{2} = c \implies \pi^* = \left( \frac{1}{2}, 1, \frac{1}{2} \right)$ .

Normalizing it we get the final result:

$$\boxed{\pi = \frac{1}{2} \left( \frac{1}{2}, 1, \frac{1}{2} \right)}$$

# 5 Simulation of a 2D Ising model by the Metropolis algorithm

## 5.1 Exercise

Using C, I have written a program that simulates the 2D Ising model with periodic boundary conditions. At first, the dimension  $L$  of the square lattice is chosen and then the initial configuration is randomly set.

At each iteration the Metropolis algorithm is used: a random number  $n \in \{0, N - 1\}$  is drawn representing one of the spins in the  $L \times L = N$  square lattice.

The energy

$$E(\mathcal{C}) = -J \sum_{\langle r_i r_j \rangle} \sigma_{r_i} \sigma_{r_j}$$

of the initial configuration, where  $\sigma_{r_i} = \pm 1 \forall i$  and  $\langle r_i r_j \rangle$  is the sum on nearest neighbors (4 in this case), is computed once and then the

$$\Delta E = 2J\sigma_{r_k} \sum_l \sigma_{r_l}$$

is calculated at each step. If  $\Delta E < 0$  or  $\log(u) < -\beta\Delta E$ , where  $u$  is a random number in  $[0, 1]$ , the new configuration with spin  $\sigma_{r_k}$  flipped is accepted, otherwise nothing changes.

At each MonteCarlo (MC) step, so after having applied the Metropolis algorithm  $\mathcal{O}(N)$  times, I have computed useful physical quantities such as the energy per spin

$$\mathcal{H} = \frac{E}{N}$$

and the magnetization per spin

$$m = \frac{\mathcal{M}}{N} = \frac{1}{N} \sum_i \sigma_i.$$

Overall, the number of MC steps is  $t_{MC} = 10^6$ .

## Simulations

Assuming  $k_B = 1$  and  $J = 1$ , I have run different simulations at different temperatures and lattice size. For each  $L \in \{25, 50, 100\}$  chosen, simulations have been run below the critical temperature  $T_b = 0.1 \cdot T_c$ , close to it  $T = 0.9 \cdot T_c$  and above it  $T_a = 2 \cdot T_c$  with  $T_c = \frac{2J}{k_B \log(1+\sqrt{2})}$ .

### Below $T_c$

Below the critical temperature we expect to observe a ferromagnetic regime, with both magnetization and energy converging to their final stationary value. This is indeed what it can be seen in the following plots where all the spins are aligned either all upward (+1) or downward (-1).

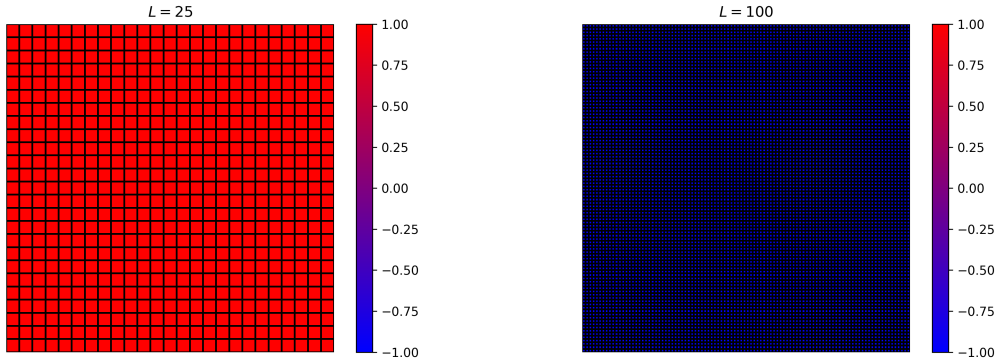


Figure 5.5: Different lattice sizes  $L = 25, 100$  at  $T_b = 0.1 \cdot T_c$

For each of these simulations, the equilibrium time  $\tau_{eq}$  has been determined:

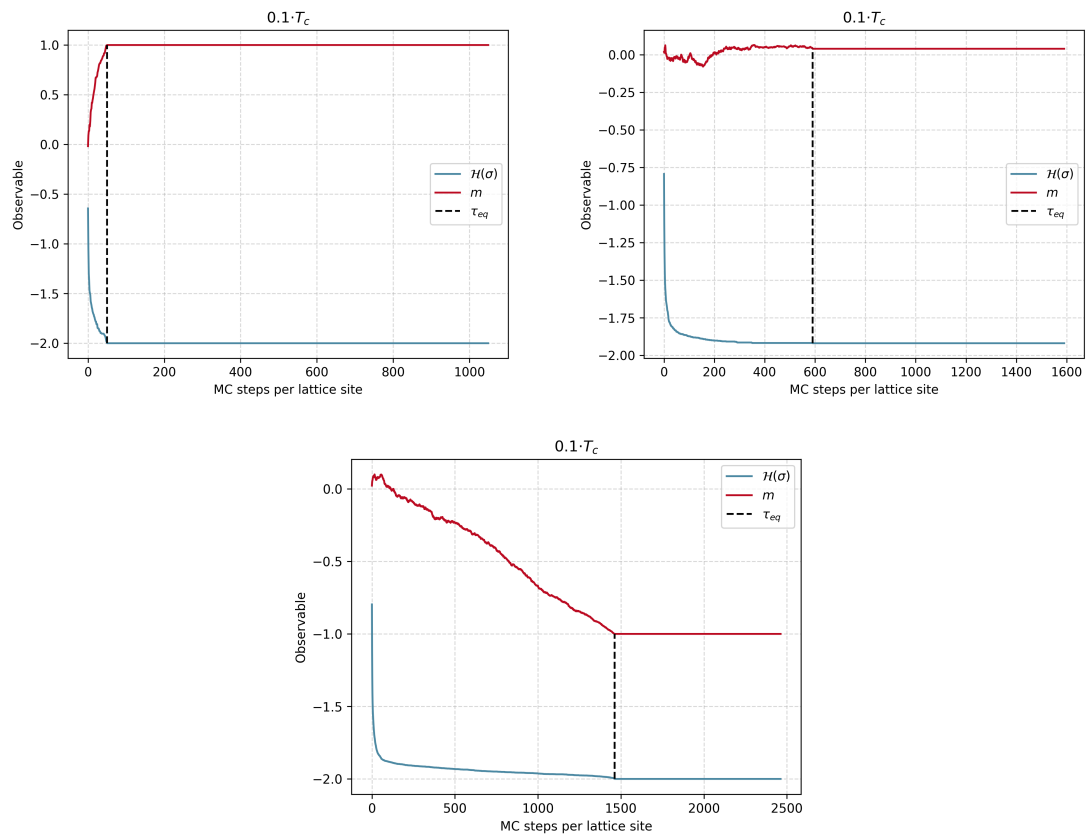


Figure 5.6: From left to bottom different lattice sizes  $L = 25, 50, 100$  respectively at  $T_b = 0.1 \cdot T_c$ ,  $\tau_{eq}$  for both  $m$  and  $E$

Table 5.1:  $\tau_{eq}$  for  $T_b$  for different  $L$

$T_b$	$L = 25$	$L = 50$	$L = 100$
$\tau_{eq}$ [MC steps]	$5.0 \cdot 10$	$6.0 \cdot 10^2$	$1.5 \cdot 10^3$

As one can expect, the larger  $L$  the higher  $\tau_{eq}$ .

## Close to $T_c$

Close to the critical temperature we still expect to observe a ferromagnetic regime, with both magnetization and energy converging to their final stationary value but in a longer  $t_{MC}$  steps. This is indeed what is shown in the following plots. The main difference from those plotted before is that the observables fluctuates much more, but eventually a stationary condition is reached with all the spins aligned either upward (+1) or downward (-1).

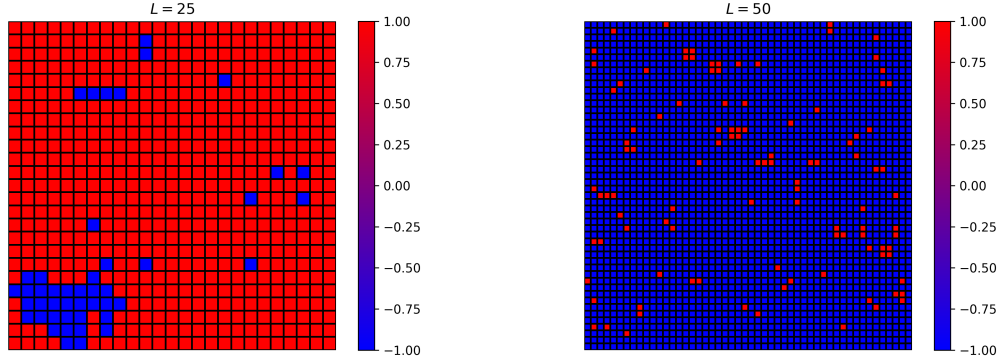


Figure 5.7: Different lattice sizes  $L = 25, 50$  respectively at  $T = 0.9 \cdot T_c$

For each of these simulations, the equilibrium time  $\tau_{eq}$  has been determined:

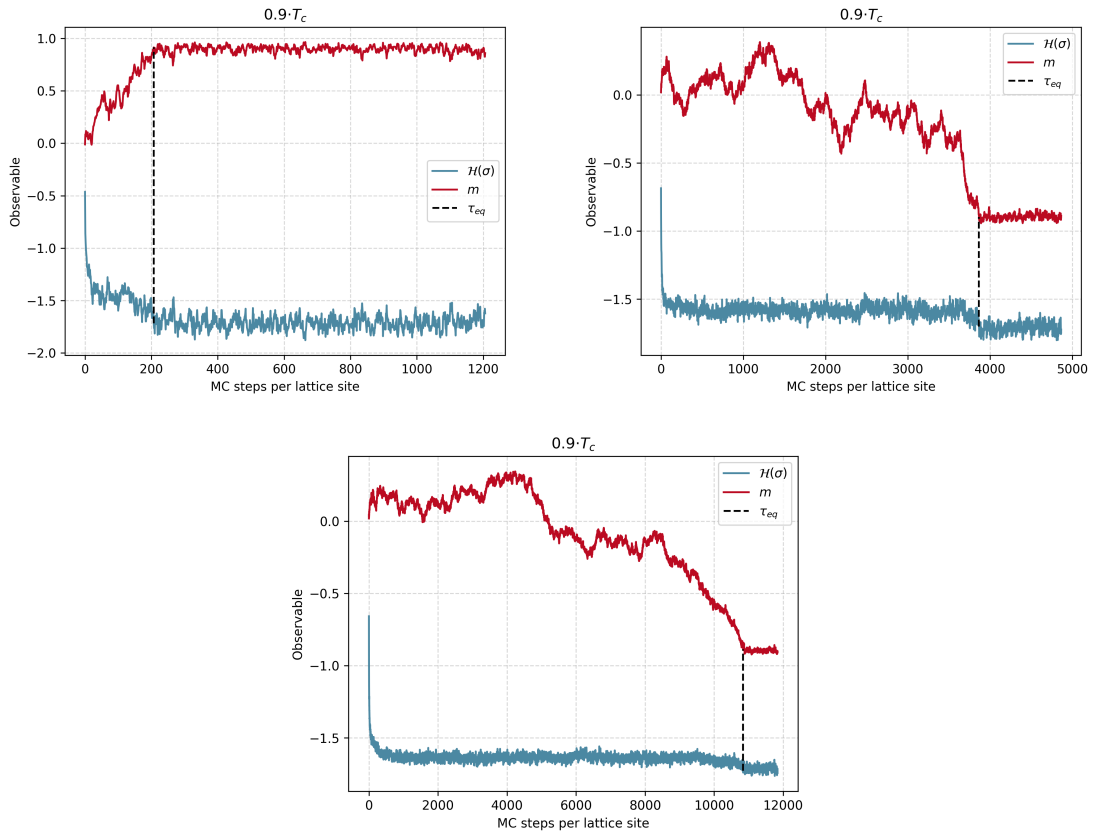


Figure 5.8: From left to bottom different lattice sizes  $L = 25, 50, 100$  respectively at  $T = 0.9 \cdot T_c$ ,  $\tau_{eq}$  for both  $m$  and  $E$

Table 5.2:  $\tau_{eq}$  at  $T = 0.9 \cdot T_c$  for different  $L$

$T = 0.9 \cdot T_c$	$L = 25$	$L = 50$	$L = 100$
$\tau_{eq}$ [MC steps]	$2.0 \cdot 10^2$	$3.9 \cdot 10^3$	$1.1 \cdot 10^4$

### Above $T_c$

Above the critical temperature the expected behaviour is purely paramagnetic, with neither local or global order. This is exactly what is shown below. Spins are not globally aligned up or down and the magnetization per spin fluctuates around zero.

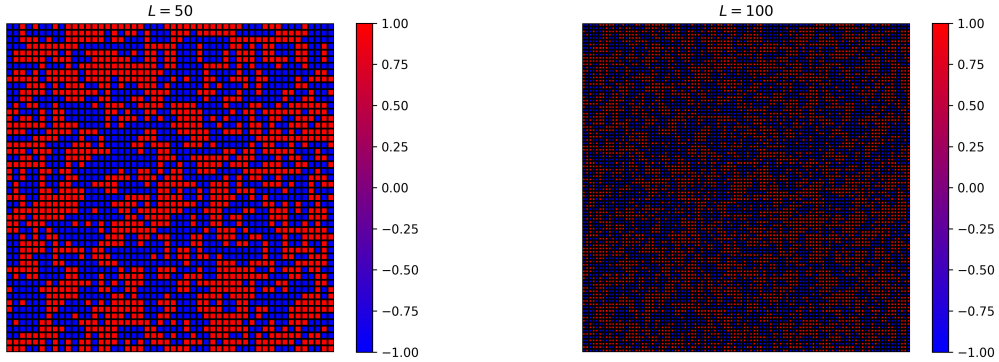


Figure 5.9: Different lattice sizes  $L = 50, 100$  respectively at  $T_a = 2 \cdot T_c$

For each of these simulations, the equilibrium time is very close to  $\sim 1$ , due to high fluctuations.

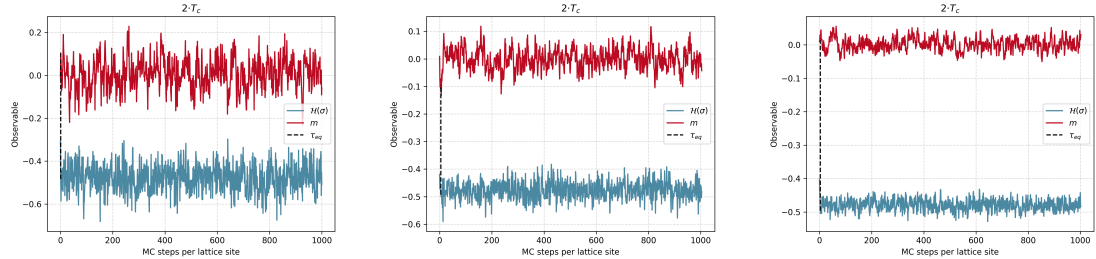


Figure 5.10: From left to bottom different lattice sizes  $L = 25, 50, 100$  respectively at  $T_a = 2 \cdot T_c$ ,  $\tau_{eq}$  for both  $m$  and  $E$

## 5.2 Exercise

### Integrated correlation time

For all of these simulations the autocorrelation function has been computed as

$$C_O(t) = \frac{1}{t_{max} - t} \sum_{t'=0}^{t_{max}-t} O(t')O(t'+t) - \frac{1}{(t_{max} - t)^2} \sum_{t'=0}^{t_{max}-t} O(t') \sum_{t'=0}^{t_{max}-t} O(t'+t)$$

Knowing that

$$C_O(t) \sim e^{-\frac{t}{\tau_{int}^O}},$$

integrating

$$\int_0^{t_{max}} \frac{C_O(t)}{C_O(0)} dt = \tau_{int}^O$$

we get immediately the integrated autocorrelation time of the observable  $O$ .

With these results, the number of measures of  $O$  that can be considered uncorrelated has been evaluated as

$$n_{uncorr}^O = \frac{t_{max}}{\tau_{int}^O}$$

The observables  $O$  considered are, as already mentioned, the energy per spin  $\mathcal{H}$  and the magnetization per spin  $m$ . Of course for the following analysis

$$\tau_{int} = \max(\tau_{int}^{\mathcal{H}}, \tau_{int}^m)$$

These results had allowed furthermore to determine the error of the mean of  $t_{max} - \tau_{eq}$  defined as

$$S_{t_{max}}^2 = \frac{1}{t_{max} - \tau_{eq} - 1} \sum_{t=\tau_{eq}}^{t_{max}} (O_t - \bar{O}_{t_{max}})^2$$

Results are presented in the following tables. All the analysis has been performed as shown in the `plots.py` and `analysis.py` files.

Table 5.3: Results for  $L = 25$

	$T = 0.2 \cdot T_c$	$T = 0.9 \cdot T_c$	$T = 2 \cdot T_c$
$\mathcal{H}$	-2.00	-1.71	-0.48
$S_{t_{max}}^{\mathcal{H}}$	0.00	0.60	0.14
$C_V$	0.00	0.82	0.12
$m$	1.00	0.90	0.00
$S_{t_{max}}^m$	0.00	0.50	0.16
$\chi_T$	0.00	0.54	0.73
$\tau_{int}$	$2 \cdot 10^1$	$3 \cdot 10^1$	$6 \cdot 10^0$
$n_{uncorr}$	$1 \cdot 10^1$	$1 \cdot 10^0$	$1 \cdot 10^2$

Here

$$C_V = \frac{\text{Var}(E)}{k_B T^2}$$

is the specific heat, and

$$\chi_T = \frac{\text{Var}(\mathcal{M})}{k_B T}$$

the magnetic susceptibility.

Table 5.4: Results for  $L = 50$

	$T = 0.2 \cdot T_c$	$T = 0.9 \cdot T_c$	$T = 2 \cdot T_c$
$\mathcal{H}$	-1.91	-1.71	-0.48
$S_{t_{max}}^{\mathcal{H}}$	0.00	2.00	0.06
$C_V$	0.00	0.81	0.12
$m$	0.04	-0.90	0.00
$S_{t_{max}}^m$	0.00	1.00	0.08
$\chi_T$	0.00	0.55	0.73
$\tau_{int}$	$5 \cdot 10^2$	$2 \cdot 10^3$	$1 \cdot 10^1$
$n_{uncorr}$	$2 \cdot 10^2$	$1 \cdot 10^0$	$2 \cdot 10^3$

And finally, for  $L = 100$ :

Table 5.5: Results for  $L = 100$

	$T = 0.2 \cdot T_c$	$T = 0.9 \cdot T_c$	$T = 2 \cdot T_c$
$\mathcal{H}$	-2.00	-1.71	-0.48
$S_{t_{max}}^{\mathcal{H}}$	0.00	0.60	0.03
$C_V$	0.00	0.81	0.12
$m$	-1.00	-0.90	0.00
$S_{t_{max}}^m$	0.00	0.40	0.01
$\chi_T$	0.00	0.54	0.74
$\tau_{int}$	$6 \cdot 10^2$	$6 \cdot 10^2$	$1 \cdot 10^0$
$n_{uncorr}$	$2 \cdot 10^1$	$2 \cdot 10^1$	$9 \cdot 10^3$

For all simulations  $t_{MC}^{max} = 10^6$  with the spins evolving as shown below:

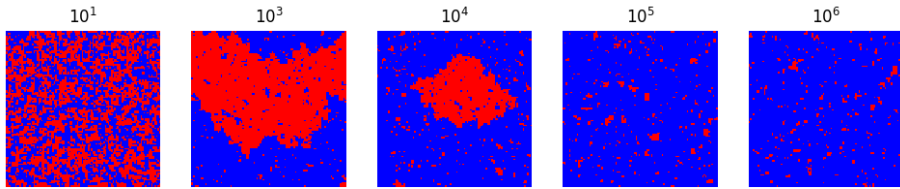


Figure 5.11: Evolution of the configuration spin values on a  $L^2 = 100 \times 100$  square lattice at  $T = 0.9 \cdot T_c$

## Finite size scaling

Following the procedure sketched in class, I have performed a finite size scaling analysis of the magnetization and the magnetic susceptibility in order to find the  $\beta$  and  $\gamma$  critical exponents.

From theory, it follows that

$$\frac{\mathcal{M}(T)}{V} = \frac{\mathcal{M}(T)}{N} = m(T) \xrightarrow{L \rightarrow \infty} L^{-\beta/\nu}$$

$$\frac{\chi(T)}{V} = \frac{\chi_{tot}(T)}{N} = N \cdot \frac{Var(m(T))}{k_B T_c} = N \chi(T) \xrightarrow{L \rightarrow \infty} L^{\gamma/\nu}$$

The estimate of the critical exponents has been performed by linearizing these relations:

$$\log(m(T)) = a \cdot \log(L) + b$$

$$\log(N \chi(T)) = c \cdot \log(L) + d$$

where in this case  $b$  and  $d$  are just two constants of proportionality and

$$a \simeq -\frac{\beta}{\nu} = -\frac{1}{8} = -0.125$$

and

$$c \simeq \frac{\gamma}{\nu} = \frac{7}{4} = 1.75,$$

having considered the exact Onsager solution with  $\boxed{\nu = 1}$ .

Since we are close to critical temperature, we change the dimension of the square lattice  $L$  and fit consequentially.

Two main problems arise: the first is that as  $L$  increases, more computational time is needed in order to retrieve an adequate value of  $m(T)$ .

The second problem is that at  $T_c$  the magnetization per spin presents very big fluctuations and its

stationary value is not as easy to predict as when working at temperatures below the critical one. Therefore,  $m$  has been computed as the average of the absolute value (since both configurations with all spins up or down represent an order phase) of the magnetization sampled after every MC step, for a total of  $10^6$  # sweeps for small  $L$  and for larger  $L = 100, 150, 200$  up to  $10^8$  total sweeps.

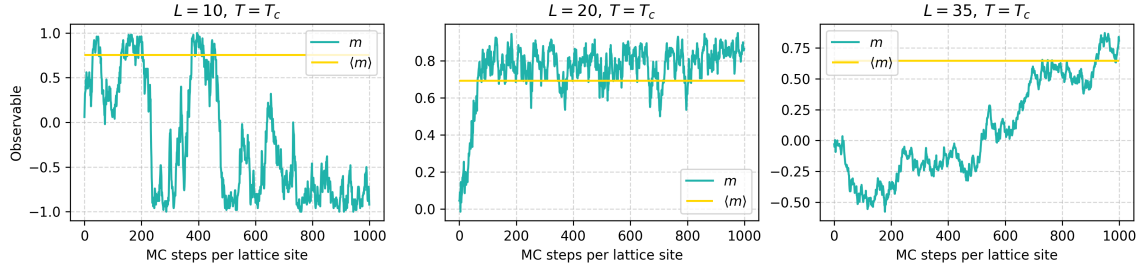


Figure 5.12: Behaviour of the average magnetization  $\langle m \rangle$  with the increase of  $L$  at  $T = T_c$ . Only the first  $10^3$  points are here presented

The linear fitting shows the estimate of the  $\beta$  and  $\gamma$  critical exponents.

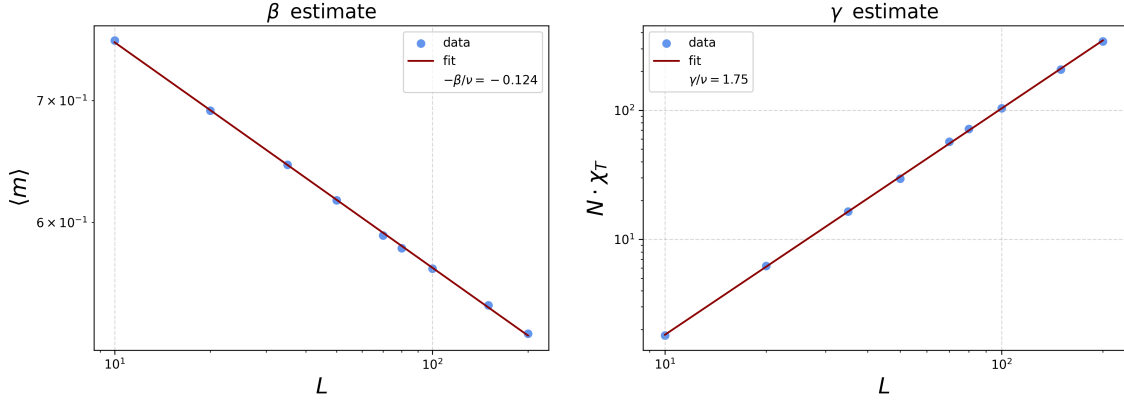


Figure 5.13:  $\beta$  and  $\gamma$  critical exponents estimate

Table 5.6: Fit results

$-\beta/\nu$	$\gamma/\nu$
-0.124	1.75

# 6 Advanced simulation of a 2D Ising model

## 6.3 Exercise: Wolff cluster algorithm

The Wolff algorithm has been implemented in C in order to properly simulate the 2D Ising model on a square lattice of linear dimension  $L$  with periodic boundary conditions. In the analysis,  $L = 50$  is kept fixed and the initial configuration is randomly set. Then, at each iteration a random number between 0 and  $N - 1$  is extracted ( $N = L \times L$ ) and the cluster starts to be originated.

### Cluster size

The cluster sizes  $\mathcal{S}(\beta)$  have been collected at three different temperatures:  $T_b = T_c/2$  below the critical temperature,  $T = T_c$  at the critical temperature and  $T_a = 2T_c$  above it.

As expected, at  $T_a$  an ordered phase is established in just few iterations. The cluster size histogram presents essentially a single bin of size  $N$ , representing the fact that it's very unlikely that just a few spins are flipped, but rather probable to flip all the lattice changing the overall magnetization per spin  $\hat{\downarrow}$  from  $-1$  to  $+1$  or viceversa.

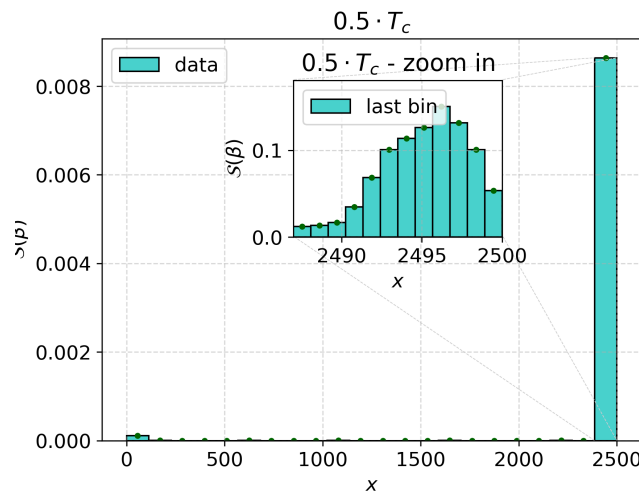


Figure 6.14: Cluster size histogram at  $T_a = 0.5 \cdot T_c$ .

Increasing the  $T$ , at the critical temperature there is no longer a global ordered phase. The cluster size histogram represents indeed a bimodal shape, with a main peak for small sizes and other smaller ones for larger sizes. This behaviour highlights the fact that at criticality it is more probable to flip small clusters, rather than the whole lattice. The latter behaviour is completely lost when the temperature is further raised, up to  $T_a = 2 \cdot T_c$  where the distribution is nothing else than an exponential decay, showing that bigger clusters are basically never flipped.

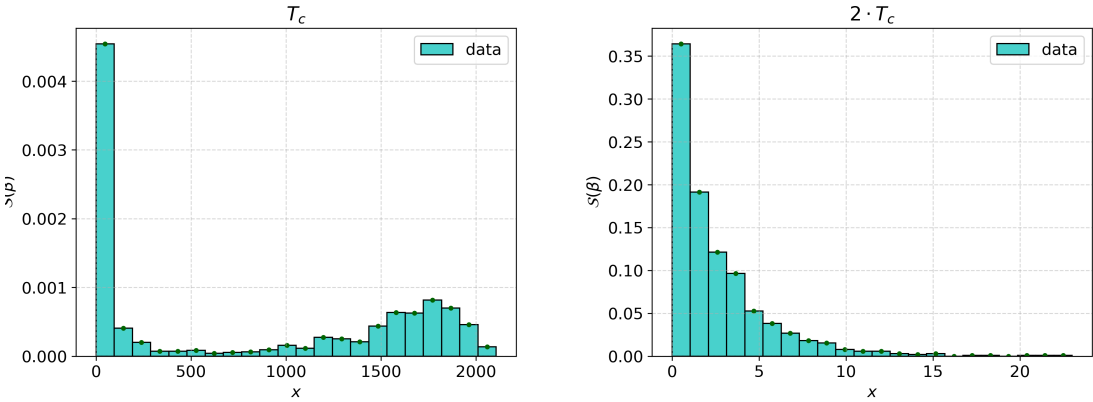


Figure 6.15: Cluster size histogram at  $T = T_c$  (left) and  $T_b = 2 \cdot T_c$  (right.)

The animation shows the cluster formation at the critical temperature every  $10^2$  iterations. If the animation is not displayed correctly, it is possible to watch them [here](#) and [here](#).

Figure 6.16: Wolff algorithm for square lattices at  $T = T_c$  (left) and  $T_a = 2 \cdot T_c$  (right)

### Autocorrelation time

The autocorrelation time  $\tau$  for a single spin flip algorithm, such as the Metropolis algorithm, scales as  $\tau \sim L^z$  where  $z$  is the dynamical critical exponent,  $z = 2$  for the 2D Ising model. The Wolff algorithm foresee a  $z_W = 0.25$ , improving the efficiency of a single spin flip algorithm by performing clusters/non-local flips.

In order to give an estimate of the  $z$  dynamical exponent for both the algorithms, I have performed simulations at different  $L$  working at  $T_c$ . The first problems I encountered are related to finite size scaling effects, which are not negligible as the linear lattice dimension is small. Looking in literature, I have found the precious paper "*Bounded and Inhomogeneous Ising Models. Specific-Heat Anomaly of a Finite Lattice*" from *A. E. Ferdinand and M. E. Fisher* in which they provide a correction to the theoretical critical temperature of the 2D Ising model, in order to reduce finite size effects. What they claimed is that  $T_c(L)$  is a function of  $L$  and the best way to find it is by looking at the peak of the specific heat. They proved that

$$T_c - T_c(L) \sim L^{-1/\nu}$$

Given  $\nu = 1$ , they pointed out that the critical temperature for a finite lattice of linear dimension  $L$  is actually above the theoretical one and scales as the inverse of the linear dimension itself. They even proposed a proportionality constant  $a(\xi)$  of this scaling.

In following their approach, I wasn't able to get any meaningful results, until I read the comment of a user <sup>(1)</sup> who essentially suggested to multiply the Ferdinand-Fisher constant by a factor 4.

---

<sup>(1)</sup>Wolff discussion

This suggestion allowed me to give a very rough estimate of the dynamical critical exponent, after countless simulations and attempts.

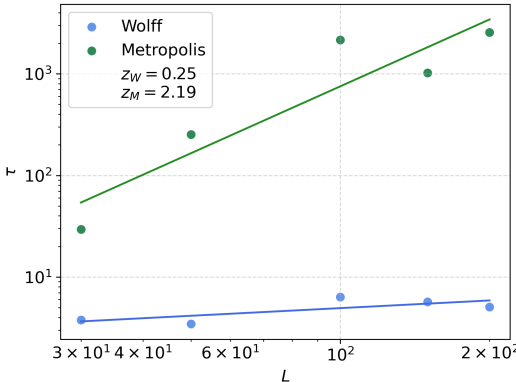


Figure 6.17:  $z$  estimate for the Ising model with local and non-local update algorithms.

The above figure is a coarse estimate of the dynamical exponent  $z$  for both the Wolff and Metropolis algorithms.  $z_W = 0.25$  is in astonishing agreement with the predicted theoretical one, thanks to an overall good scaling of  $\tau_W$ , i.e. the fit is not very good but all the points, especially at high  $L$ , seem to follow the predicted exponential law.

It is worth to mention that after having calculated  $\tau_{data}$ ,  $\tau$  is given by

$$\tau \simeq \tau_{data} \frac{\mathcal{S}(\beta)}{L^2}$$

But at the critical temperature the cluster size distribution presents a bimodal behaviour (see *left* Figure [6.15]). The average cluster size  $\mathcal{S}(\beta)$  would be in this case something in between two peaks. Since at the critical temperature we expect not to observe long range order, the results shown in the above plot are computed by considering only an average on the left hand side of the  $\mathcal{S}(\beta)$  distribution, where indeed one can examine low cluster dimension formation, so low presence of nearby spins of the same sign.

As to the Metropolis algorithm the behaviour of  $z_M \simeq 2$  is reached: the low  $L$  simulations push this estimate even further the theoretical expected one.

To conclude, the result shown can be easily better presented by, for instance, simulating a fair number of times the very same systems in order to get also an estimate of the error bars of the points plotted and then evaluating their agreement with respect to the fitted line.

## 6.4 Exercise: Multiple Markov Chains

Keeping  $L = 50$  fixed, I have implemented 5 Markov chains for the Ising model, at different consecutive temperatures:

$$T_1 = 0.5 \cdot T_c, \quad T_2 = 0.8 \cdot T_c, \quad T_3 = T_c, \quad T_4 = 1.5 \cdot T_c, \quad T_5 = 2 \cdot T_c.$$

Dealing with multiple Markov Chains, the possibility to swap from a chain  $i$  to a chain  $j$  if and only if  $|i - j| = 1$  (so for nearby chains) has been introduced, with a swapping rate  $\sim 20\%$ , as suggested.

The two plots below show the behaviour of the magnetization per spin and the energy per spin as time passes. It is immediate to see the big jumps in both observables, making evident the effect of swapping among nearby chains. On the *left* ( $T_2 = 0.8 \cdot T_c$ ), for example, the high (low) peaks in the magnetization (energy) could have been given by a swap with chain 1 ( $T_1 = 0.5 \cdot T_c$ ), while fluctuations around the dotted black line - so lower magnetizations - could have been brought by a swap from the third chain ( $T_3 = T_c$ ).

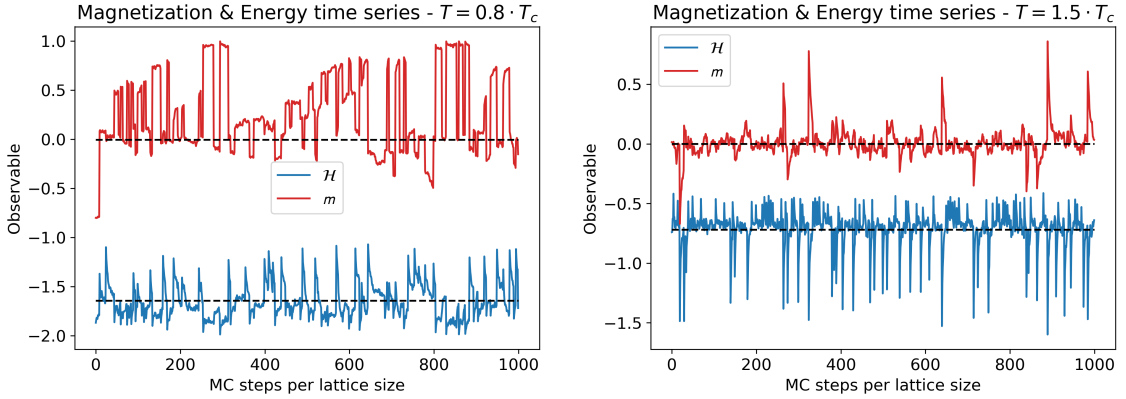


Figure 6.18: Magnetization and energy per spin fluctuations in the last  $10^3$  MC sweeps.

As expected, energy distributions of nearby chains are overlapped, testifying to the exchange that took place between neighboring chains.

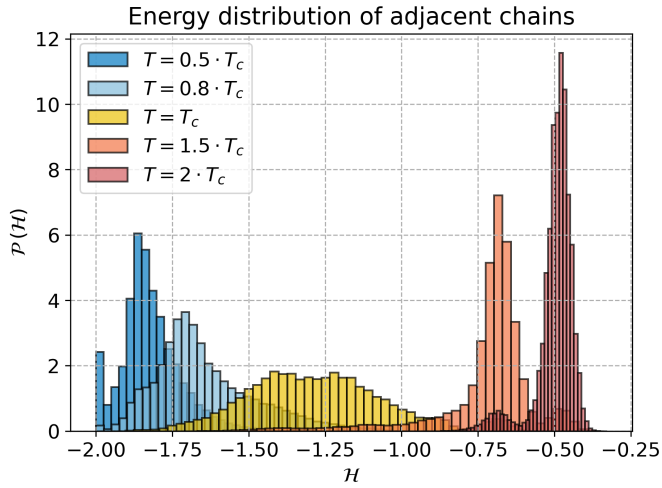


Figure 6.19: Overlapping of the energy per spin distribution for adjacent chains.

Furthermore, the swapping rates between chains has been kept track of. The figures below represent the *escaping rate* from a chain  $i$  to be swapped to any other chain  $j$ . So for example, the first chain can only go into the second one, while the latter can only be swapped with the first or the third one, and so on. As shown, the swapping rate  $\sim 20\%$  on average.

The *right* plot instead represents the *incoming rate*, so the rate at which a generic chain  $j$  is swapped into the  $i$ -th considered (of course  $i \neq j$ ). The picture demonstrate the behaviour of the middle chains (second and fourth chains) as a bridge between ordered/critical and unordered phases.

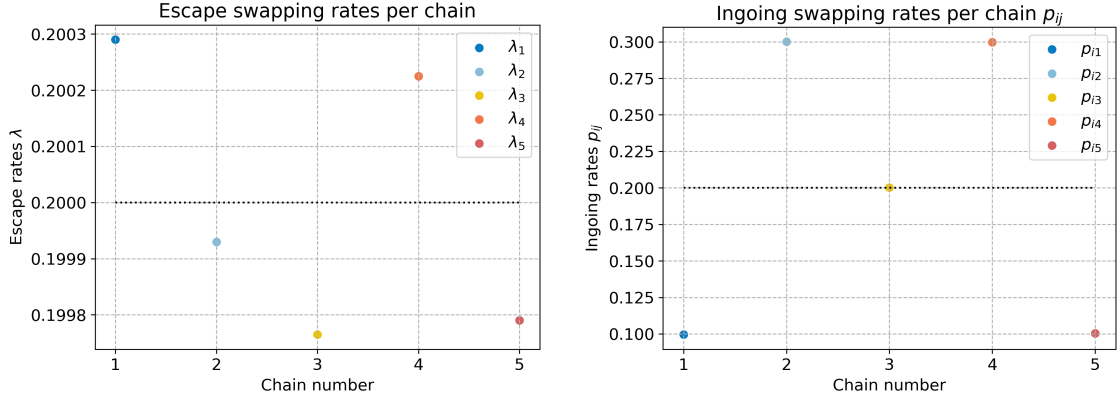


Figure 6.20: *Escaping* and *ingoing* rates per Markov Chain.

Moreover, the autocorrelation time per chain has been exploited and compared with the very same Markov Chains but where swapping is not allowed.

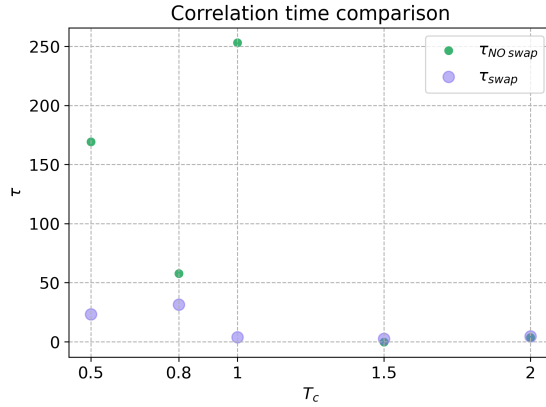


Figure 6.21:  $\tau$  comparison for swapping and non-swapping MMC

It is immediate to observe how the MMC model allows to reduce correlation between samples, especially for  $T \leq T_c$ . Above  $T_c$ , samples are overall uncorrelated due to high fluctuations in the observables since no ordered phase exists, regardless of the possibility to swap chains.

# 7 Continuous time Markov processes

The Gillespie algorithm has been developped so to implement both *Lotka-Volterra* and the *Brusselator* models.

## 7.5 Lotka - Volterra

The *Lotka-Volterra* model has been simulated considering the parameters  $k_1 = 3 \text{ s}^{-1}$ ,  $k_2 = 0.01 \text{ s}^{-1}$  and  $k_3 = 5 \text{ s}^{-1}$ .

The Gillespie algorithm allows to produce stochastic dynamics which are in good agreement with the numerical solutions of the system.

Starting near the equilibrium point  $\mathcal{C}^* = \mathcal{C}(0) = (k_3/k_2, k_1/k_2)$  one can see that system remains very close to this equilibrium point.

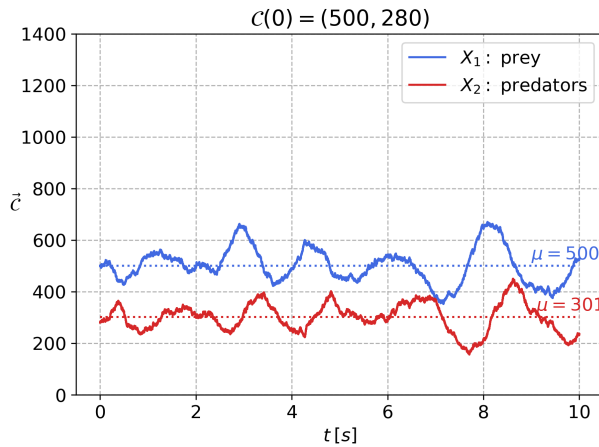


Figure 7.22: *Lotka-Volterra* simulation with Gillespie algorithm starting close to the equilibrium point

Far from  $\mathcal{C}^*$  the dynamics becomes unstable and presents periodic oscillations. Starting from a number of *preys* higher than *predators*, one can see immediately how their number tends to raise until the number of *predators* starts to increase in the same manner. When  $X_2 \gg X_1$ , there are not enough *preys* to feed all the *predators*, so the dynamics reverses back.

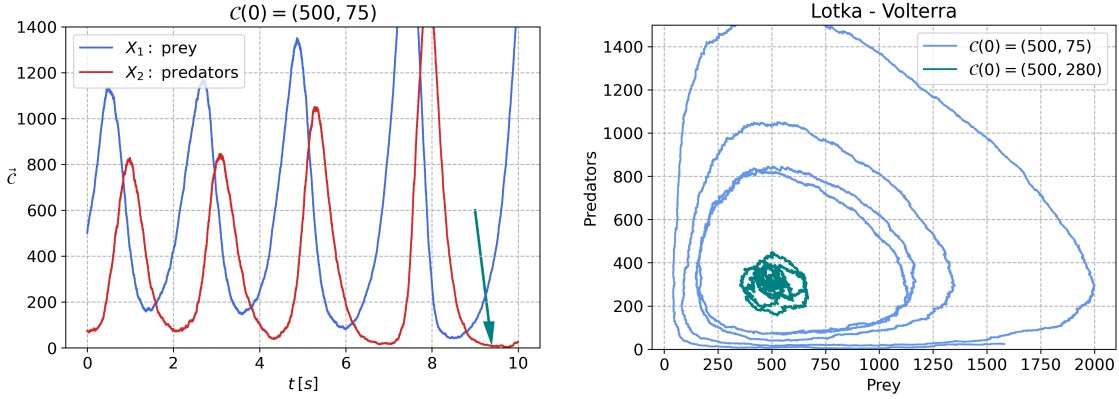


Figure 7.23: *Lotka-Volterra* simulation with Gillespie algorithm far from  $\mathcal{C}^*$

The *predators* never becomes extinct completely but the above *left* plot points out a situation in which their population gets very close to zero. In this case, the population of *preys* explodes. This is something explicable directly by the rate equations of the model since when  $X_2 \rightarrow 0$ , the evolution growth of  $X_1$  is exponential. To prevent this behaviour one has to tune the constant rates  $k_R$ . An higher  $k_3$ , for example, promotes the death of *predators*, while an higher  $k_2$  promotes interaction between species, benefiting *predators* to the detriment of *preys*. By evaluating the Jacobian at  $\mathcal{C}^*$  one finds that the two eigenvalues are

$$\lambda_{1,2} = \pm i\sqrt{k_3 k_1},$$

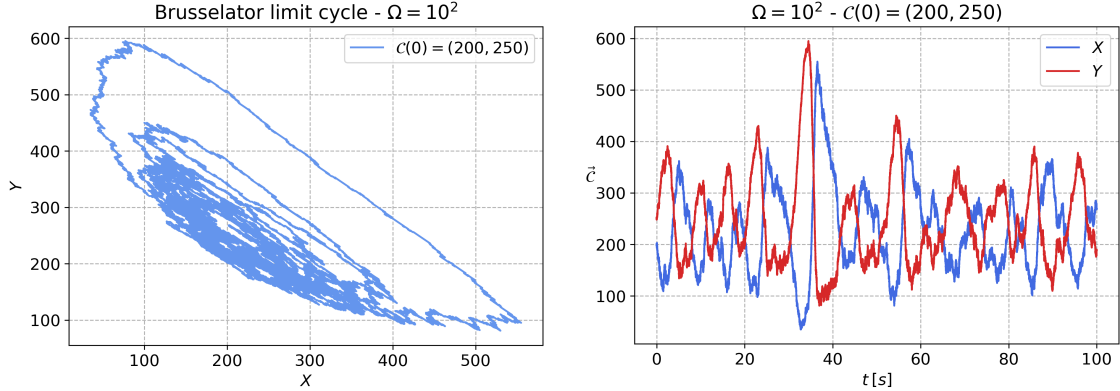
thus leading to an oscillatory dynamics. If one imposes one of the two rates  $k_1$ ,  $k_3$  to be zero, we get a degenerate dynamics with two identical eigenvalues of the Jacobian equal to zero. As a result, preys will die due the competition term  $\propto -k_2 X_2$ , provoking then the extinction of predators too.

The expected oscillatory dynamics of *preys* ( $X_1$ ) and *predators* ( $X_2$ ) is plotted too on the *right*. The limit cycle in the phase diagram is there highlighted.

## 7.6 Brusselator

Setting  $a = 2$   $b = 5$ , the Gillespie algorithm has been implemented to perform simulations of the *Brusselator* model for different volume sizes  $\Omega$ .

For each volume, the starting configuration  $\mathcal{C}(0)$  has been set to  $X = a \cdot \Omega$  and  $Y = \frac{b}{a} \cdot \Omega$ .



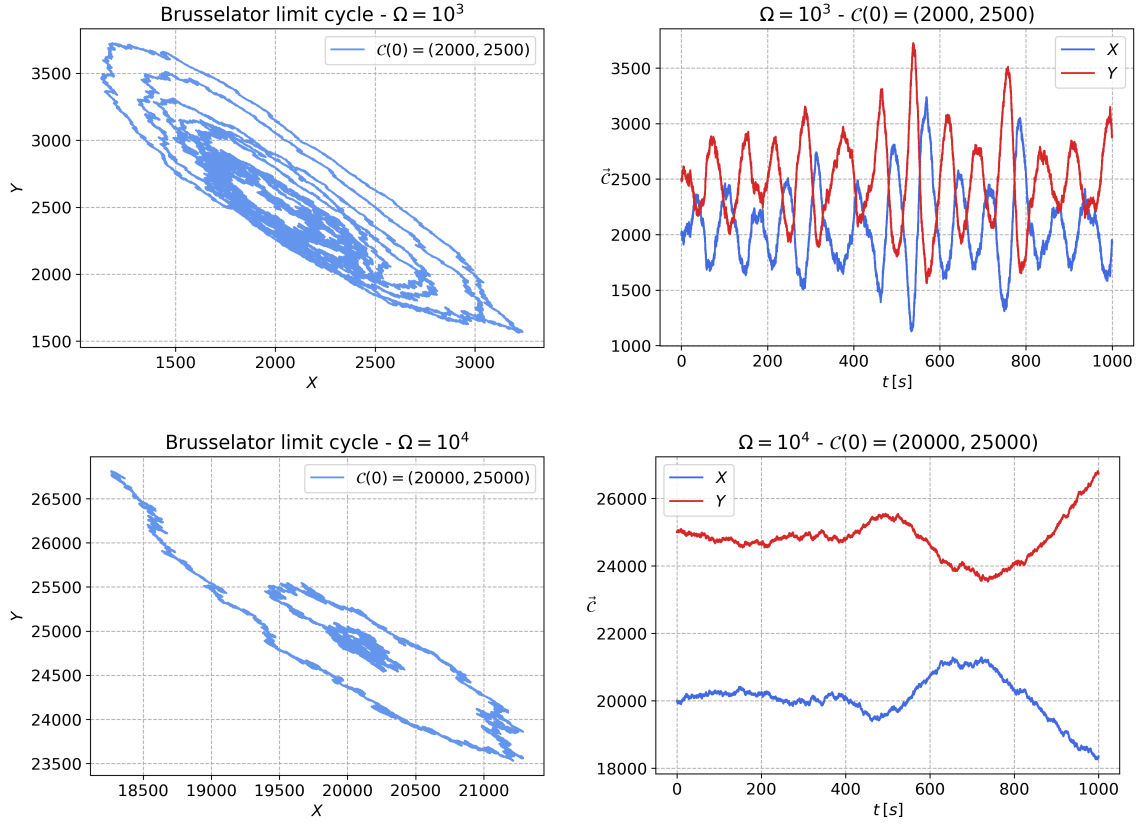


Figure 7.24: *Brusselator* model for volume size  $\Omega = 10^2$  (top panels),  $\Omega = 10^3$  (middle panels) and  $\Omega = 10^4$  (bottom panels)

By increasing  $\Omega$  one can note that the time required for the simulation to form the stochastic limit cycle increases.

All these runs have been realized considering a total time  $t_{max} = 10^3$  s and proceeding at a  $dt = 10^{-3}$ . For small volumes ( $\Omega = 10^2$ ) one can see that just after  $50 - 60$  s the limit cycle originates and the dynamics becomes oscillatory. The very same behaviour can be observed for  $\Omega = 10^3$ , shifted in time by a factor 10. In just  $\sim 100$  s one would not be able to observe any oscillatory behaviour in the middle panels, as witnessed by the bottom plots at  $\Omega = 10^4$  where  $10^3$  s are not enough to observe any oscillations in the stochastic dynamics.

# 8 Off-lattice simulations: basics

## 8.7 Exercise: Reduced units

Using the typical sets of parameters for *Argon*  $\sigma_{Ar} = 3.41\text{\AA}$  and *Krypton*  $\sigma_{Kr} = 3.38\text{\AA}$ , one can compute the quantities of interest:

- Given the reduced temperature  $T^* = 2$  and  $\varepsilon_{Ar}/k_B = 119.8K$ ,  $\varepsilon_{Kr}/k_B = 164.0K$  the temperature of *Argon* can be computed as:

$$\begin{aligned} T_{Ar} &= \alpha \frac{E_{Ar}}{k_B} \stackrel{(a)}{=} E_{Ar}^* \left( \frac{\varepsilon_{Ar}}{k_B} \right) \alpha \stackrel{(b)}{=} \alpha \left( \frac{\varepsilon_{Ar}}{k_B} \right) \frac{T^*}{\alpha} \\ &= \left( \frac{\varepsilon_{Ar}}{k_B} \right) T^* = 2 \cdot 119.8 K = 239.6 K \end{aligned}$$

and similarly for *Krypton*:

$$T_{Kr} = \left( \frac{\varepsilon_{Kr}}{k_B} \right) T^* = 2 \cdot 164.0 K = 328.0 K$$

where in (a) I used the definition of reduced units:

$$E^* = \frac{E}{\varepsilon} \quad (8.1)$$

and in (b) what comes from reduced units application:

$$E^* = \frac{T^*}{\alpha} \quad (8.2)$$

- Using the typical value of the integration time step  $\Delta t = 0.001\tau \implies \Delta t^* = 10^{-3}$  and recalling that

$$\tau = \sqrt{\bar{m}\sigma^2/\varepsilon},$$

one can compute the integration time step in **SI** units. Indeed, setting the reduced mass  $m^* \stackrel{!}{=} 1$  then  $\bar{m}$  is given by:

$$\bar{m} = \frac{m}{m^*} \implies \begin{cases} \bar{m}_{Ar} = m_{Ar} \simeq 2Z_{Ar} u \\ \bar{m}_{Kr} = m_{Kr} \simeq 2Z_{Kr} u \end{cases}$$

where  $Z_{Ar} = 18$ ,  $Z_{Kr} = 36$  and  $u = 1.66 \cdot 10^{-27} \text{ Kg}$  is the mass of a proton. Using the definition of  $\tau$ :

$$\tau = \sqrt{\bar{m}\sigma^2/\varepsilon} \implies \begin{cases} \tau_{Ar} = \sqrt{\bar{m}_{Ar}\sigma_{Ar}^2/\varepsilon_{Ar}} = 2.1 \cdot 10^{-12} \text{ s} \\ \tau_{Kr} = \sqrt{\bar{m}_{Kr}\sigma_{Kr}^2/\varepsilon_{Kr}} = 2.5 \cdot 10^{-12} \text{ s} \end{cases}$$

and finally:

$$\Delta t = 10^{-3} \cdot \tau \implies \begin{cases} \Delta t_{Ar} = 10^{-3} \cdot \tau_{Ar} = 2.1 \cdot 10^{-15} \text{ s} \\ \Delta t_{Kr} = 10^{-3} \cdot \tau_{Kr} = 2.5 \cdot 10^{-15} \text{ s} \end{cases}$$

- The friction coefficient  $\gamma$  is given by the Stokes' law:

$$\gamma = 6\pi\eta r$$

and since  $[\eta] = \mathbb{P} \cdot \mathbb{T} = \frac{\mathbb{M}}{\mathbb{T} \cdot \mathbb{L}}$ , then  $[\gamma] = \frac{\mathbb{M}}{\mathbb{T}}$ .

Therefore, it is possible to define  $\gamma^*$  as:

$$\gamma^* = \gamma \cdot \frac{\tau}{m} = \frac{\gamma}{m} \sqrt{\frac{m\sigma^2}{\varepsilon}} = \boxed{\gamma \sqrt{\frac{\sigma^2}{m\varepsilon}}}$$

and  $\eta^*$  as:

$$\eta^* = \eta \cdot \frac{\tau\sigma}{m} = \frac{\eta\sigma}{m} \sqrt{\frac{m\sigma^2}{\varepsilon}} = \boxed{\frac{\eta\sigma^2}{\sqrt{m\varepsilon}}}.$$

## 8.8 Exercise: Off lattice Monte Carlo of Hard Spheres

Following the instructions provided, the off lattice Monte Carlo algorithm has been implemented to recover the Hard Spheres model in Soft Matter. For a system of  $N = 100$  particles, I have tested the performances of the model at different density values:

$$\rho = \frac{N}{V} = 0.01, 0.3, 0.5, 1$$

and for different maximum displacement:

$$d_{max} = 0.01 \cdot \sigma, 0.05 \cdot \sigma, 0.3 \cdot \sigma, 0.5 \cdot \sigma, 1 \cdot \sigma$$

in terms of **acceptance ratio** and **energy** evolution through time. Through the whole computation I have set as suggested  $\sigma \stackrel{!}{=} 1$ .

- Starting from a completely random lattice, I run different simulations in order to understand how the acceptance rate and the energy change when  $\rho$  and  $d_{max}$  vary.

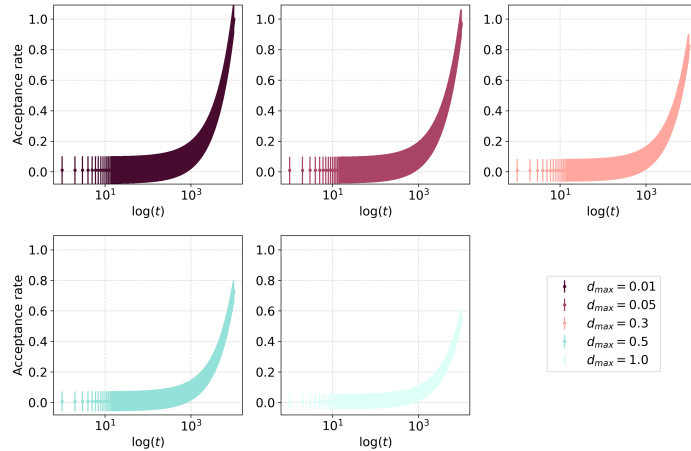


Figure 8.25: Acceptance rate as a function of time and  $d_{max}$ ,  $\boxed{\rho = 0.3}$

The plot above shows an average - over 10 different initial configurations - of the evolution of the acceptance ratio per  $10^4$  timesteps. Overall, the number of accepted moves increases as  $t \gg 1$  due to convergence of the algorithm. This convergence is faster for smaller  $d_{max}$  for the specific  $\rho = 0.3$  shown. As  $\rho$  gets smaller, the change in  $d_{max}$  is not relevant and the behaviour of the acceptance ratio is overall the same. Indeed, due to the high volume available, any move basically results in a decrease in the quantity of *overlap*. The energy therefore reaches

its minimum almost immediately even with the most randomic initial configuration since the  $N$  particles are all at a distance  $d > \sigma$ .

For higher values of  $\rho$  - so for smaller volumes available - there are higher fluctuations in the acceptance rate. Indeed, the picture below shows that the energy stays almost everywhere the same for large  $d_{max}$  and it decreases only after a huge number of steps for smaller  $d_{max}$ .

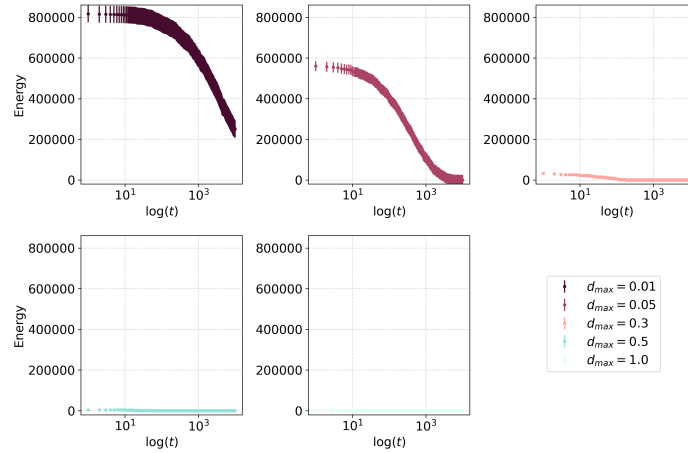


Figure 8.26: Energy as a function of time and  $d_{max}$ ,  $\rho = 0.5$

- The case of a cubic crystal with a primitive cell of fixed length is a better approach to the problem. The acceptance rate grows faster for smaller  $d_{max}$  since there is already an available space, while for larger  $d_{max}$  the acceptance rate is lower since a move closer to  $\sigma$  is very unlikely to be accepted.

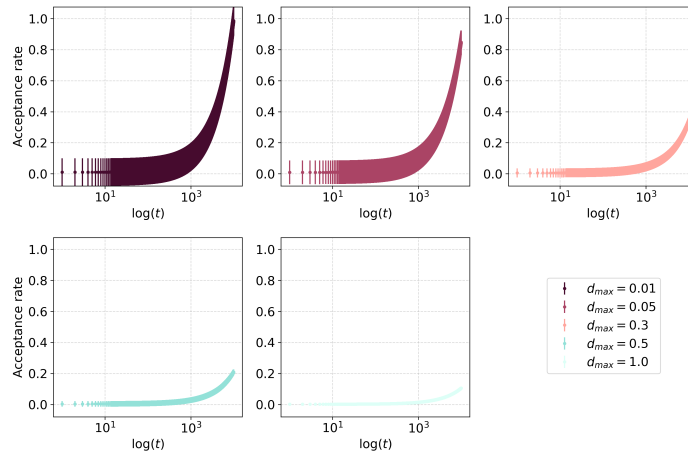


Figure 8.27: Acceptance as a function of time and  $d_{max}$ ,  $\rho = 1$

## 8.9 Exercise: Off lattice Monte Carlo of Lennard Jones particles

Similarly, the Lennard - Jones potential has been implemented in combination with the two tail corrections proposed. Two sets of simulations have been performed and compared with the provided results: one above the critical temperature  $T^* = 2$  and another one at  $T^* = 0.9$ , below  $T_c$ . This time, the number of particles has been set to  $N = 200$ .

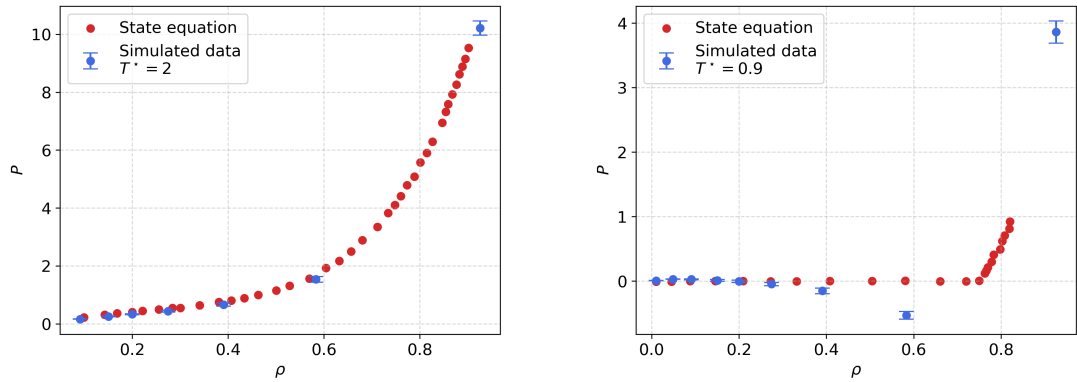


Figure 8.28: Pressure-density plot below the reduced critical temperature  $T^* = 0.9$  (*left*) and above the reduced critical temperature  $T^* = 2$  (*right*)

There is good agreement between the provided data and those estimated. Each plotted point in *blue* is an average over 10 different realizations of the system, left to evolve for  $10^4$  timesteps.

Below the reduced critical temperature, the expected behaviour of the pressure is found with its peculiar negative behaviour due to the coexistence of two phases.

# 9 Integration schemes

## 9.10 Exercise: Harmonic Oscillators

- a) Expressing the equations in matrix form one is able to show that for one integrator  $\det M > 1$ , while for the other  $\det M = 1$ .

$$\begin{cases} p(t + \Delta t) = p(t) - x(t)\Delta t \\ x(t + \Delta t) = x(t) + x(t)\Delta t \end{cases} \implies \begin{pmatrix} x \\ p \end{pmatrix}_{(t+\Delta t)} = \underbrace{\begin{pmatrix} 1 & \Delta t \\ -\Delta t & 1 \end{pmatrix}}_M \begin{pmatrix} x \\ p \end{pmatrix}_{(t)} \quad (9.3)$$

and one can see immediately that

$$\det M = 1 + (\Delta t)^2 > 1, \quad \forall \Delta t > 0.$$

The second integrator is an Euler symplectic integrator of the first order.

$$\begin{cases} p(t + \Delta t) = p(t) - x(t)\Delta t \\ x(t + \Delta t) = x(t)(1 - (\Delta t)^2) + p(t)\Delta t \end{cases} \implies \begin{pmatrix} x \\ p \end{pmatrix}_{(t+\Delta t)} = \underbrace{\begin{pmatrix} 1 - (\Delta t)^2 & \Delta t \\ -\Delta t & 1 \end{pmatrix}}_M \begin{pmatrix} x \\ p \end{pmatrix}_{(t)} \quad (9.4)$$

which leads to

$$\det M = 1 - (\Delta t)^2 + (\Delta t)^2 = 1.$$

The property pointed out by these calculations is the symplectic nature of the latter algorithm which preserves the volume information of the system, as one would expect by an Hamiltonian system.

- b) To prove that the latter integrator has the shadow Hamiltonian

$$H' = H - \frac{px}{2}\Delta t$$

as constant of motion one can proceed in different ways. One way is to verify that:

$$H'(t + \Delta t) = H'(t)$$

To do so:

$$\begin{aligned} H'(t + \Delta t) &= H(t + \Delta t) - \frac{p(t + \Delta t)x(t + \Delta t)}{2} \\ &= \frac{x(t + \Delta t)^2}{2} + \frac{p(t + \Delta t)^2}{2} - \frac{p(t + \Delta t)x(t + \Delta t)}{2} \\ &= \frac{1}{2}x(t)^2(1 - \Delta t^2)^2 + p(t)^2\Delta t^2 + 2p(t)x(t)(1 - \Delta t^2)\Delta t + \\ &\quad - \frac{1}{2}p(t)^2 + x^2\Delta t^2 - 2p(t)x(t)\Delta t - \frac{1}{2}(p(t) - x(t)\Delta t)(x(t)(1 - \Delta t^2) + p(t)\Delta t)\Delta t \\ &= \dots = \frac{x^2}{2} + \frac{p^2}{2} - \frac{xp}{2}\Delta t \\ &= H(t) \end{aligned}$$

- c) Both integrators have been used to calculate the solution of the proposed harmonic oscillator with initial conditions  $x(0) = 1$  and  $p(0) = 0$ .

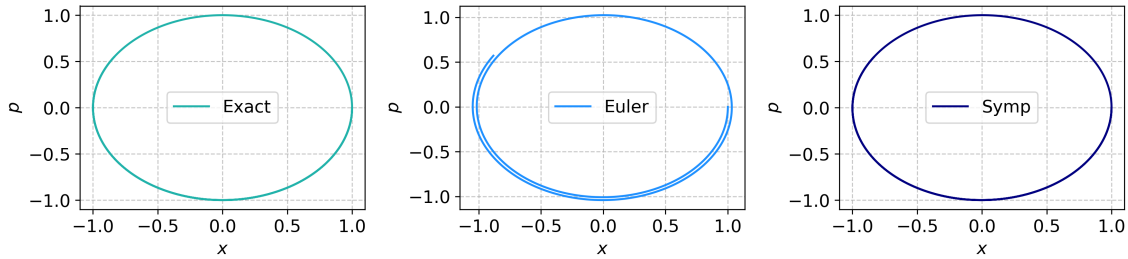


Figure 9.29: Comparison of the phase space between exact solution (*left*) Euler method Eq:[9.3] (*middle*) and Symplectic integrator Eq:[9.4] (*right*) for  $\Delta t = 10^{-2}$

In the above plot the comparison between the different methods is presented with integration time  $\Delta t = 10^{-2}$ . It is clear immediately that the Euler method [9.3] is not very precise.

I now plot the error, for simplicity, just defined as the difference between the integrators output and the real solution:

$$\varepsilon = x_{\text{integ}} - x_{\text{exact}}.$$

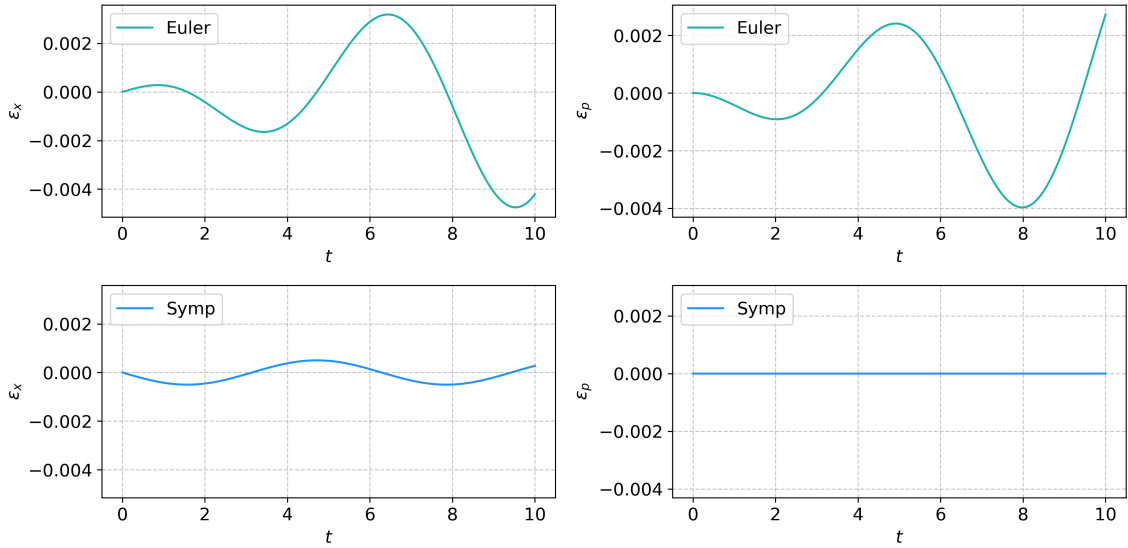


Figure 9.30: Difference between integrators output and real solution with  $\Delta t = 10^{-3}$

One can see immediately that for the presented case of  $\Delta t = 10^{-3}$  the Symplectic integrator Eq:[9.4] is more robust and closer to the real solution. Furthermore, oscillations are confined and they do not increase as  $t$  gets larger.

- d) The same behaviour can be analyzed by plotting the Hamiltonian:

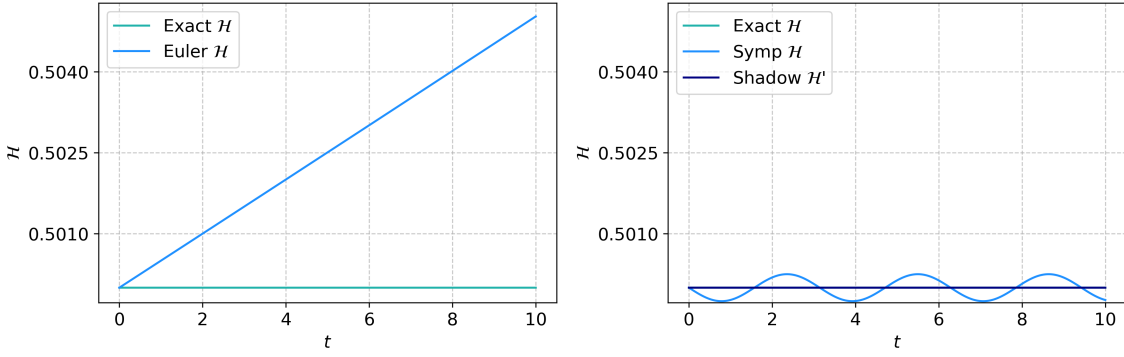


Figure 9.31: Hamiltonian comparison between numerical integrators and exact solution at  $\Delta t = 10^{-3}$

Again, the Euler integrator is less accurate with respect to the Symplectic one. In the *right* plot, the shadow and exact Hamiltonians are (partially) overlapped, but one can see instantly that the drift suffered from the shadow Hamiltonian is much smaller than that suffered from the  $\mathcal{H}$  of the system Eq:[9.4], which still represents a better approximation than the Euler method Eq:[9.3].

## 9.11 Velocity Verlet integrator: the harmonic oscillator

The *Velocity Verlet* algorithm has been implemented and compared with the *Beeman* algorithm. Setting  $\omega = 1$  one is able to get the same system as the one proposed in the previous exercise, with  $\Delta t = 10^{-3}$ .

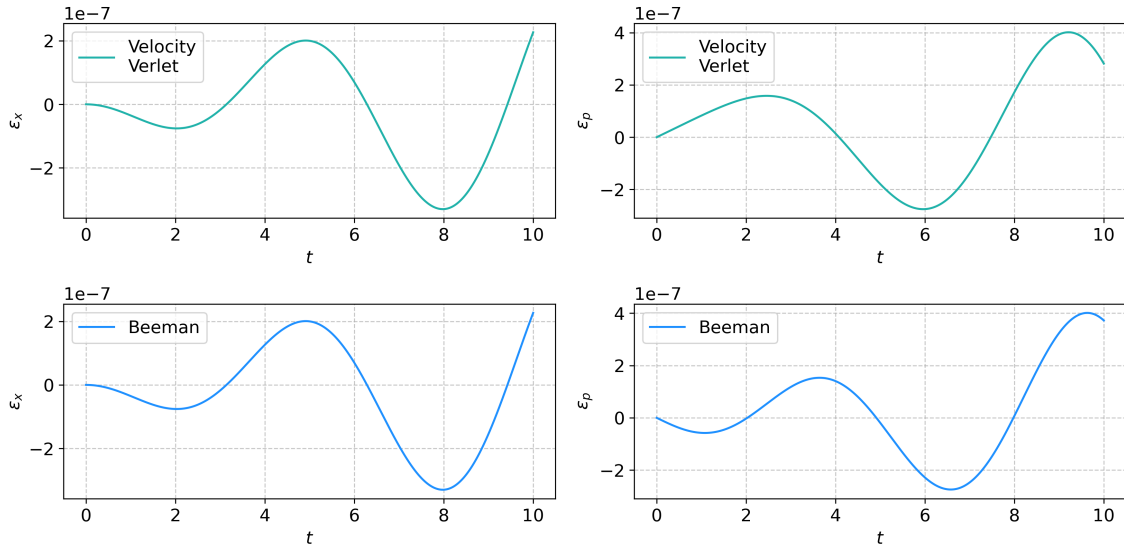


Figure 9.32: Difference between integrators output and real solution with  $\Delta t = 10^{-3}$

Looking at the  $y$  axis, one can capture the order of magnitude of the error between the algorithms and the exact solution of the harmonic oscillator ( $\varepsilon_x$  and  $\varepsilon_p$ ). Their behaviour is essentially the same, as one would expect since the Beeman algorithm can be proven to satisfy the Verlet algorithm.

Plotting instead  $(\mathcal{H}(t) - \mathcal{H}_0)/\mathcal{H}_0$  the error ( $\Delta\mathcal{H}$ ) is smaller too with respect to the integrators considered in the previous section. Both the Velocity Verlet and the Beeman algorithms present an oscillatory behaviour:  $\mathcal{H}(t)$  differs slightly from the expected one with periodic deviations which

tend to be negative in the case of the Velocity Verlet algorithm and smaller and all positive for the Beeman one.

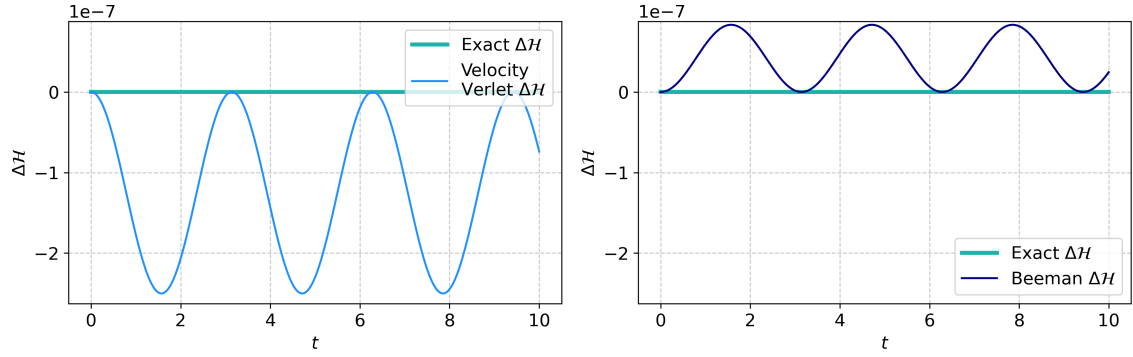


Figure 9.33: Hamiltonian comparison between numerical integrators and exact solution at  $\Delta t = 10^{-3}$

# 10 Interaction potentials & thermostats

## 10.12 Exercise: Canonical fluctuations

Recalling the general expression for the energy for a system of  $N$  particles in the canonical ensemble, one is able to write

$$\langle T_k \rangle = \frac{2}{3Nk_B} \langle E_k \rangle$$

and therefore related the given expression with the energy fluctuations:

$$\frac{\sigma_{T_k}^2}{\langle T_k \rangle^2} = \frac{\langle E_k^2 \rangle - \langle E_k \rangle^2}{\langle E_k \rangle^2} = \frac{\langle \Delta E_k \rangle^2}{\langle E_k \rangle^2}$$

The variance of the energy in this ensemble is

$$\langle \Delta E_k \rangle^2 = k_B T_k^2 \frac{\partial \langle E_k \rangle}{\partial T_k},$$

which allows us to conclude:

$$\frac{\sigma_{T_k}^2}{\langle T_k \rangle^2} = \frac{k_B T_k^2}{\langle E_k \rangle^2} \frac{\partial \langle E_k \rangle}{\partial T_k} = \frac{k_B T_k^2 \cdot \frac{3}{2} N k_B}{\frac{9}{4} N^2 k_B^2 T_k^2} = \boxed{\frac{2}{3N}}.$$

## 10.13 Exercise: Lennard-Jones fluid in the microcanonical ensemble

I have simulated  $N = 200$  particles of mass  $m = 1$  confined in a cubic box of length  $L = 10$  with periodic boundary conditions. Each particle interacts with each other with a Lennard - Jones (LJ) potential. Setting  $\sigma = 1$  and  $\epsilon = 1$ , with  $\rho = N/V = 0.2$ , I have integrated the equations of motion using the Velocity Verlet algorithm.

Starting with a well equilibrated initial condition, I have sampled the initial positions uniformly within the box  $[0, L] \times [0, L] \times [0, L]$  and the initial velocities from the equilibrium Maxwell - Boltzmann distribution with zero mean and variance  $\sqrt{T^*}$ . For this exercise I have set  $T^* = 1$  and then I enforced the total initial momentum to zero.

Later, I have performed different simulations at different  $r_c$  (LJ potential cut-off). Starting from  $r_c^{min} = 1 \cdot \sigma$ , I proceeded up to  $r_c^{max} = 4 \cdot \sigma$  with steps  $\Delta r_c = 0.2$ . The plots below show (*left*) the trend of the LJ potential through time ( $10^4$  iterations with  $dt = 10^{-3}$ ), the behaviour of the simulated  $T_k^*$  temperature (*middle*), with a black baseline corresponding to  $T^* = 1$  and finally (*right*) the radial distribution function.

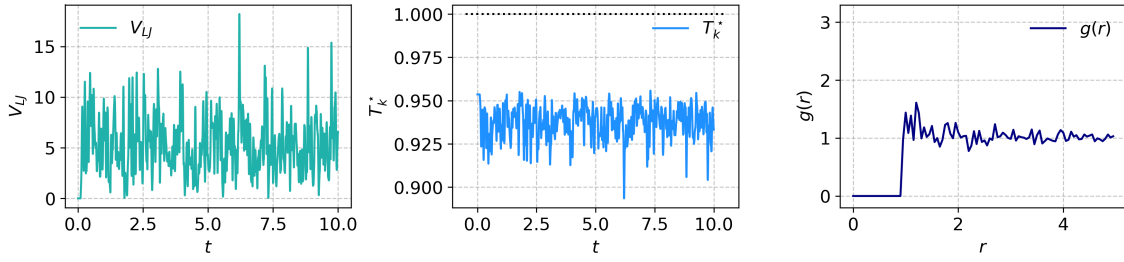


Figure 10.34: LJ potential, temperature  $T_k^*$  and RDF for  $\rho = 0.2$  with  $[r_c = 1 \cdot \sigma]$

This above panel, for example, shows different system properties: the conservation of energy, as one would expect by a symplectic algorithm such as the Velocity Verlet. The very same discussion holds for the *central* panel, showing the evolution of the temperature of the system, so the kinetic energy. In the *right* panel the radial distribution function (RDF) has been plotted, correctly normalized (its integral properly returns  $N$ , the number of particles). A more in-depth discussion follows.

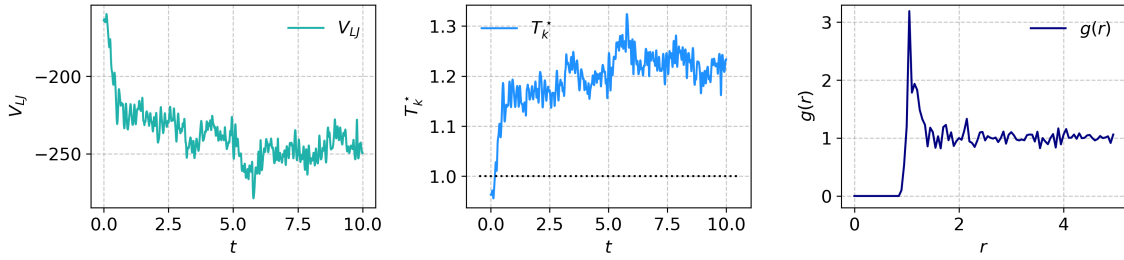


Figure 10.35: LJ potential, temperature  $T_k^*$  and RDF for  $\rho = 0.2$  with  $[r_c = 2 \cdot \sigma]$

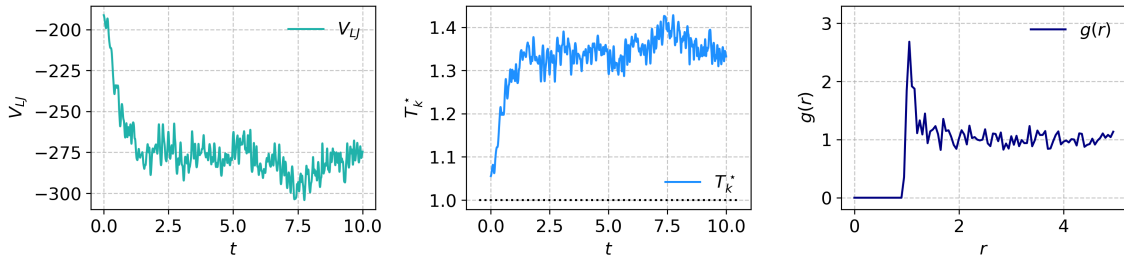


Figure 10.36: LJ potential, temperature  $T_k^*$  and RDF for  $\rho = 0.2$  with  $[r_c = 3 \cdot \sigma]$

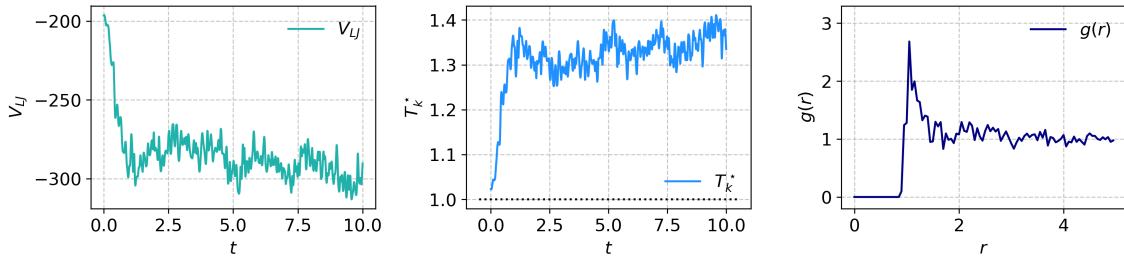


Figure 10.37: LJ potential, temperature  $T_k^*$  and RDF for  $\rho = 0.2$  with  $[r_c = 4 \cdot \sigma]$

By comparing these plots at different  $r_c$  it is immediate to visualize that as the potential cut-off raises a more prominent peak is highlighted. This peak is always at  $r \sim 2^{1/6}\sigma$ , where  $2^{1/6}\sigma$  is the minimum of the LJ potential  $r_{min}$ . The higher  $r_c$  the less the potential is truncated, allowing interaction with particles at larger distance. Overall, what these plots highlight is the higher probability of finding particles at the potential minimum. That is that particles tend to organize in small clusters of  $2 \div 3$  particles each, within the range  $r_{min} \rightarrow r_{min} + dr$ .

As  $r$  increases, the probability of finding particles oscillates around  $\approx 1$ , emphasizing the absence of some sort of order within the system.

Between the two extreme cases, for  $r \geq 2 \cdot \sigma$ , the potential allows both repulsive and (as  $r$  increases, more and more) attractive regimes with the appearance of a peak in the *RDF*.

## 10.14 Exercise A: Lennard-Jones fluid with thermostats

The same Lennard-Jones system has been simulated again but this time using two different thermostats. Having set  $T^* = 2$  for this computation and  $\sigma = 1 = r_c$ , I have computed the kinetic energy  $E_k$  in order to verify its consistency with the equipartition theorem, varying  $N \in \{80, 120, 160, 200\}$ , keeping the volume  $V$  fixed.

- **Velocity rescaling**

At each iteration, velocities have been rescaled accordingly to

$$\vec{v}' = \lambda \vec{v}$$

where

$$\lambda = \sqrt{\frac{T^*}{T_k(t)}}.$$

Thanks to this rescaling the kinetic energy is always fixed and equal to its initial value. In the end, its average  $\langle E_k \rangle$  is in perfect agreement with the expected theoretical value.

Table 10.7: Velocity rescaling: non canonical thermostat

$N$	$\langle E_k^{theor} \rangle$	$\langle E_k^{simul} \rangle$	$\left( \frac{\sigma_{T_k}^2}{\langle T_k \rangle^2} \right)^{theor}$	$\left( \frac{\sigma_{T_k}^2}{\langle T_k \rangle^2} \right)^{simul}$
80	240.0	240.0	0.0083	$\sim 10^{-31}$
120	360.0	360.0	0.0056	$\sim 10^{-31}$
160	480.0	480.0	0.0042	$\sim 10^{-31}$
200	600.0	600.0	0.0033	$\sim 10^{-31}$

As emphasized by the above table, one can see how this thermostat enforces the total kinetic energy to be fixed. As a consequence, there is perfect agreement between the simulated and theoretical predicted  $\langle E_k \rangle$  average, while the variance of the energy is null and in disagreement with that of the canonical ensemble  $\frac{\sigma_{T_k}^2}{\langle T_k \rangle^2} = \frac{2}{3N}$ , as one would expect since this is not a canonical thermostat.

- **Andersen thermostat** The frequency of collisions has been set to  $\omega = 2 \cdot 10^3$ . At each iteration a random number  $r_i \in (0, 1)$  has been assigned to each particle. If  $r_i < \omega dt$  a velocity vector  $\vec{v}_i$  is sampled from the Maxwell-Boltzmann distribution:

$$v_i \sim \mathcal{N}(\mu = 0, \sigma = \sqrt{T})$$

(indepedently for each component).

Table 10.8: Andersen canonical thermostat

$N$	$\langle E_k^{theor} \rangle$	$\langle E_k^{simul} \rangle$	$\left( \frac{\sigma_{T_k}^2}{\langle T_k \rangle^2} \right)^{theor}$	$\left( \frac{\sigma_{T_k}^2}{\langle T_k \rangle^2} \right)^{simul}$
80	240.0	240.1	0.0083	0.0083
120	360.0	360.4	0.0056	0.0056
160	480.0	480.4	0.0042	0.0042
200	600.0	600.3	0.0033	0.0033

The above table and the below plot show that the average kinetic energy is consist with the equipartition theorem as well as the temperature fluctuations of the canonical ensemble, as expected for a canonical thermostat.

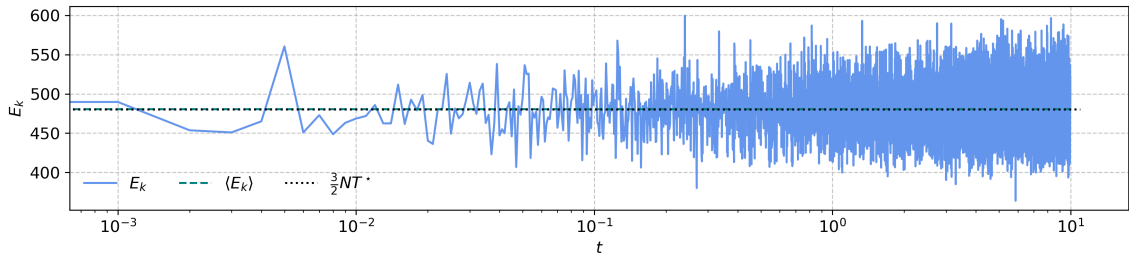


Figure 10.38: Andersen thermostat with  $N = 160$ . Dotted and dashed lines with theoretical and computed  $\langle E_k \rangle$  perfectly overlapping

# 11 Langevin and Brownian Dynamics

## 11.15 Exercise: On the validity of the Langevin approach

- The correlation time of water molecules is

$$\tau_{coll} \sim 10^{-12} \text{ s}$$

and

$$\Delta t \geq 10 \cdot \tau_{coll} \simeq 10^{-11} \text{ s}.$$

This leads to the following inequality:

$$10^{-2}\tau \geq 10^{-11} \rightarrow \tau \geq 10^{-9} \text{ s}.$$

Recalling the definition of  $\tau = \sqrt{\frac{\bar{m}\sigma^2}{\varepsilon}}$ , setting

$$\bar{m} = \rho \cdot \frac{4}{3}\pi\sigma^3$$

under the hypothesis of spherical object and using  $\rho = \rho_{H_2O} = 10^3 \text{ Kg/m}^3$  the following inequality holds:

$$\sigma \geq \sqrt[5]{(10^{-9})^2 \cdot \frac{k_B T_r}{T^*} \cdot \frac{3}{4\pi\rho}} \simeq [4 \cdot 10^{-9} \text{ m}]$$

where I used also a previously found relation:  $\varepsilon = k_B T_r / T^*$ , with  $T_r = 300 \text{ K}$  the room temperature and  $T^* = 1$ . This represents an estimation of the minimum size of the object for which the Langevin description is acceptable.

- In the overdamped limit, in  $1-d$  the diffusion coefficient is given by the mean square displacement

$$\langle (x(t) - x_0)^2 \rangle \approx 2Dt.$$

Using the Einstein relation

$$D = \frac{K_B T_r}{3\pi\eta\sigma} \approx \frac{\sigma^2}{2\Delta t}$$

and calling with  $\Delta t$  the time scale of a particle of diameter  $\sigma = 10^{-8} \text{ m}$  to diffuse in water over a distance equal to its diameter:

$$\Delta t = \frac{3\pi\eta}{2k_B T_r} \sigma^3 \simeq [10^{-6} \text{ s}]$$

where  $\eta \simeq 10^{-3} \text{ Pa} \cdot \text{s}$  for water at  $T_r = 300 \text{ K}$ . This time scale is perfectly compatible with the requirement of  $t \ll \tau_{coll}$ .

- Brownian motion becomes negligible if we work at time scales of orders of seconds. So, setting  $\Delta t \sim 1 \text{ s}$ , inverting the later equation:

$$\sigma = \sqrt[3]{\frac{2k_B T_r \Delta t}{3\pi\eta}} \simeq 10^{-6} \text{ m} = 1 \mu\text{m}$$

in agreement with the provided estimate of  $\sigma$ . In this context, the overdamped approximation is no longer valid and inertial/deterministic effects are no longer negligible.

## 11.16 Exercise: Simple Brownian motion

I considered a single isolated particle and set  $m = 1, \sigma = 1, \epsilon = 1$  as units of mass, length and energy. Then, I simulated the particle in the overdamped and underdamped limit in a box of length  $L = 20\sigma$  with periodic boundary conditions. All the presented results are an average of  $N = 200$  realizations of the same system.

### 11.16.1 Overdamped limit

I computed the mean square displacement ( $MSD$ ) varying the reduced temperature  $T^*$  within the proposed range, keeping fixed  $\gamma\tau \equiv 1$ . All the proposed results are obtained by passing from the "wrapped" coordinates of the simulation box (pbc are applied) to "unwrapped" coordinates in order to compute effectively the  $MSD$  parameter.

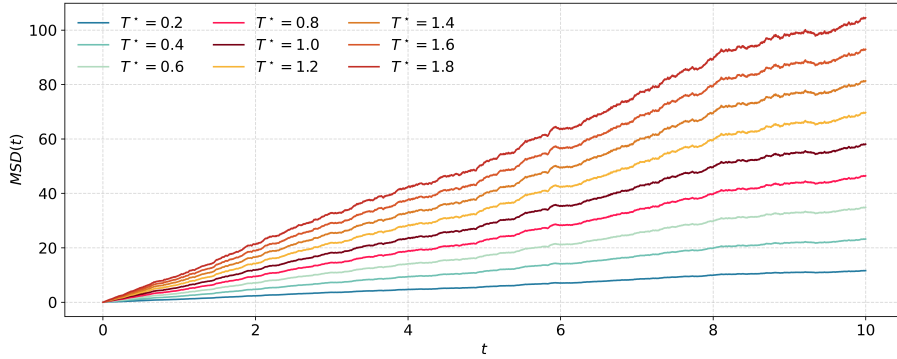


Figure 11.39: Mean square displacement in the overdamped limit as a function of the reduced temperature  $T^*$ . Average over  $N = 200$  realizations

Recalling the first order integrator of the overdamped Langevin equation

$$r(t + \Delta t) = r(t) + \frac{F(r(t))}{m\gamma} \Delta t + \sqrt{\frac{2k_B T}{m\gamma}} \Delta t \xi$$

it is clear to see that the larger the temperature  $T^* = k_B T$  the greater the fluctuations in the updated position. This translates into an higher diffusion of the particle. The temperature kicks the particle away from its initial position resulting in an increased  $MSD(T^*)$ .

Then, I computed the mean square displacement varying  $\gamma\tau$  within the proposed range, keeping fixed  $T^* \equiv 1$ .

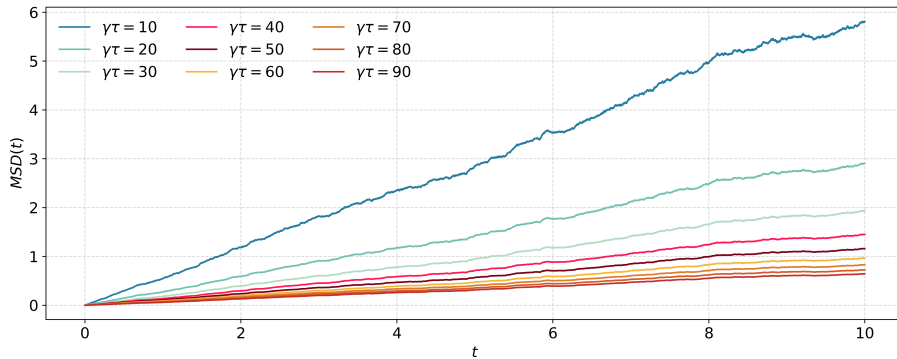


Figure 11.40: Mean square displacement in the overdamped limit as a function of the coefficient  $\gamma\tau$ . Average over  $N = 200$  realizations

Conversely, an increase in  $\gamma\tau$  at fixed  $T^* \equiv 1$  leads to a reduction of stochastic effects. The particle moves less and tends to stay closer to the initial position. This explains the lower values reached by the  $MSD$  in the above plot, with the highest slope for the lowest simulated  $\gamma\tau$ .

### 11.16.2 Underdamped limit

The very same analysis has been carried out for the underdamped case too, using the Stochastic Velocity Verlet algorithm.

Results are very similar to those shown in the previous section, but now it is possible to give an estimate of the diffusion coefficient  $D$  via the Green-Kubo relation.

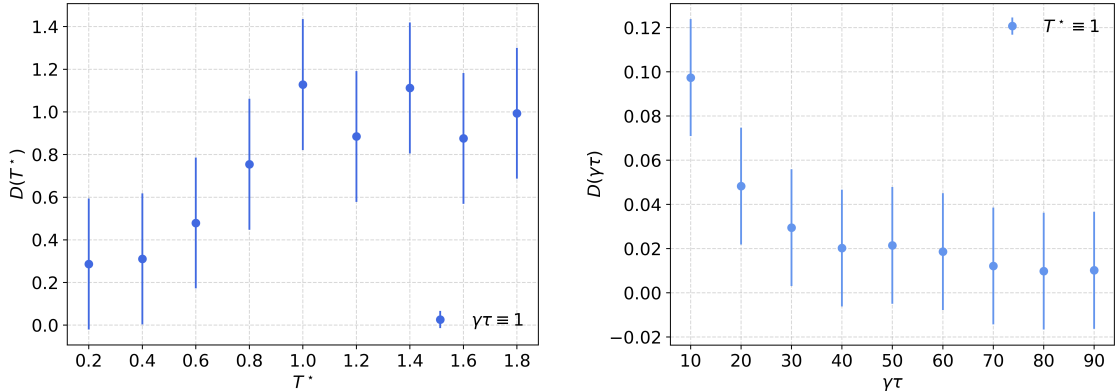


Figure 11.41: Diffusion coefficient estimate in the underdamped limit as a function of the reduced temperature  $T^*$  (left) and  $\gamma\tau$  (right). Average over  $N = 200$  realizations

The above plots show essentially a linear "fit" of the curves previously presented. Once the velocity autocorrelation function ( $VACF(\tau) = \langle \vec{v}(t_0 + \tau) \cdot \vec{v}(t_0) \rangle$ ) has been computed, the diffusion coefficient is given by the relation

$$D = \frac{1}{3} \lim_{t \rightarrow \infty} \int_0^t VACF(\tau) d\tau$$

where the factor  $1/3$  is because the simulation has been carried out in 3-dimensions.

As expected by the Einstein relation:

$$D = \frac{k_B T}{m\gamma},$$

a temperature rise leads to an increase in  $D$  (left plot), while an increment in  $\gamma$  guide to smaller values of the diffusion coefficient. The plot on the right indeed exhibits a  $1/x$  behavior, while in the left figure, the linear pattern is not well established probably due to the system not having reached stationarity within the simulated time.

### 11.17 Exercise: Overdamped colloid in an harmonic trap

I considered a single overdamped particle in an harmonic trap described by the potential

$$V(r) = \frac{1}{2} K (\vec{r} - \vec{r}_0)^2$$

with  $\vec{r}_0 = (0, 0)^T$  for simplicity. In this exercise all simulations have been performed in a 2D box of linear size  $L = 20\sigma$ . The initial position of the particle has been fixed at  $\vec{r}(t_0) = (1, 0)^T$  and velocities drawn from the equilibrium distribution.

### 11.17.1 Average positions

In the following plots, I have computed the average - over  $N = 200$  realizations of the same system - of the position of the particle along the  $x$ -axis (*left*) and  $y$ -axis (*right*) as a function of temperature  $T^*$ , friction  $\gamma\tau$  and spring stiffness  $K\sigma^2/\epsilon$ . When varying one quantity, the other two were kept fixed to unitary value.

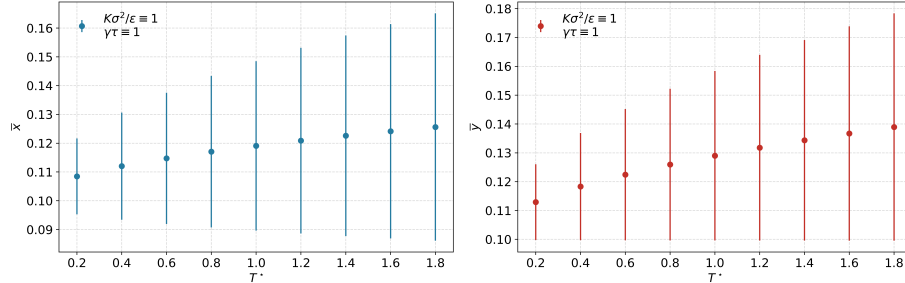


Figure 11.42: Average and standard deviation of the particle position in the overdamped limit as a function of the reduced temperature  $T^*$ . Average over  $N = 200$  realizations

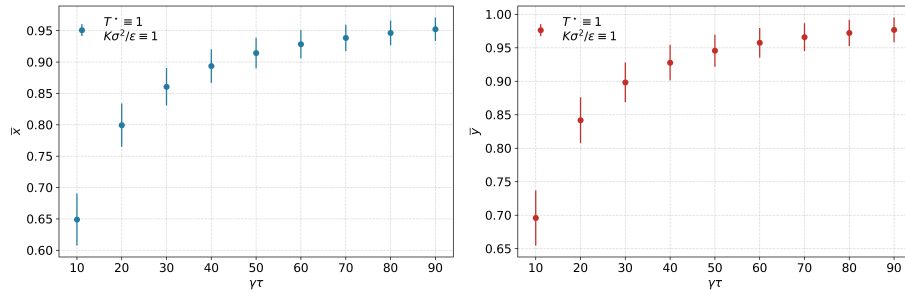


Figure 11.43: Average and standard deviation of the particle position in the overdamped limit as a function of  $\gamma\tau$ . Average over  $N = 200$  realizations

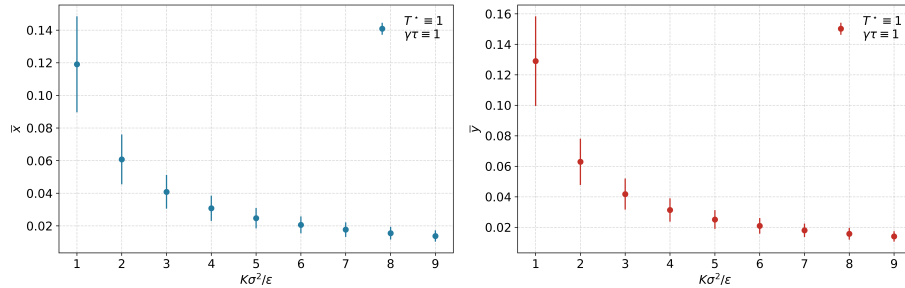


Figure 11.44: Average and standard deviation of the particle position in the overdamped limit as a function of  $K\sigma^2/\epsilon$ . Average over  $N = 200$  realizations

Trends for both examined axes are very similar. Higher variances are encountered when varying the temperature which is indeed the parameter enhancing fluctuations.

Higher distances are instead traveled when the friction coefficient  $\gamma$  is enlarged, as expected, since higher  $\gamma$  translates into a weaker force contribution into the system's dynamics.

The opposite conclusion can be made for the third panel, where  $T^*$  and  $\gamma$  are fixed and  $K$  is varied. A larger  $K$  imposes a constraint on the system which is less prone to move, due to the high spring stiffness. The particle therefore tends to move closer to the rest location of the spring.

### 11.17.2 Time correlation of particle-probe distance

A very similar behavior can be observed from the time correlation of the distance between the particle and the center of the probe at equilibrium. The  $y$ -axis of the following plots showing  $\bar{\tau}_x$  on the left and  $\bar{\tau}_y$  on the right are rescaled to the simulation time, multiplying by the simulation time step  $dt = 10^{-3}$ . The distance time correlation decreases as noise raises, as one would expect, so when  $T^*$  increases or  $\gamma$  decreases or when  $K$  is enhanced, promoting a deterministic dynamics rather than a stochastic one.

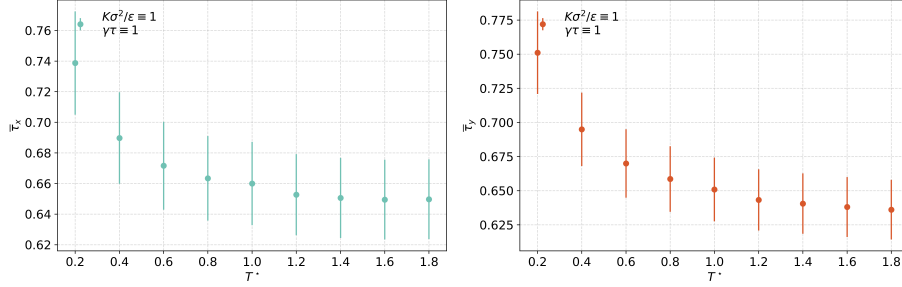


Figure 11.45: Time correlation of the distance between the particle and the probe positions in the overdamped limit as a function of  $T^*$ . Average over  $N = 200$  realizations

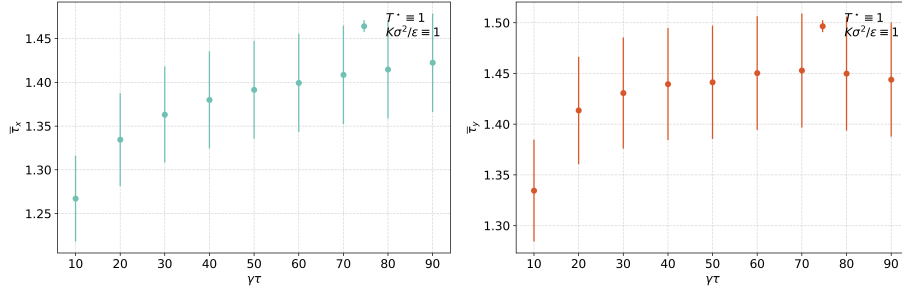


Figure 11.46: Time correlation of the distance between the particle and the probe positions in the overdamped limit as a function of  $\gamma\tau$ . Average over  $N = 200$  realizations

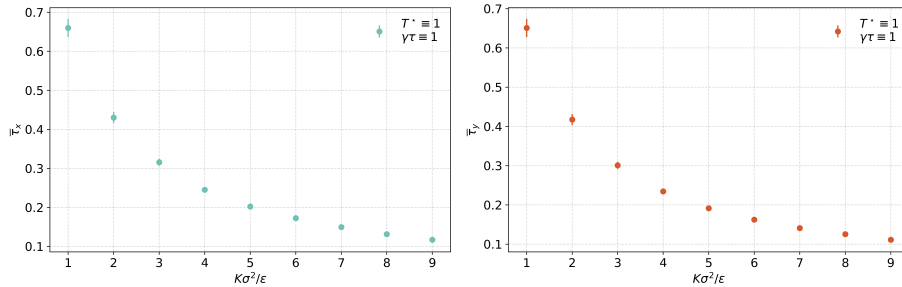


Figure 11.47: Time correlation of the distance between the particle and the probe positions in the overdamped limit as a function of  $K\sigma^2/\epsilon$ . Average over  $N = 200$  realizations

### 11.17.3 Double harmonic trap

I set another trap at a distance  $2\sigma$  from the first one: more precisely,  $\vec{r}_0^{(1)} = (0, 0)^T$  and  $\vec{r}_0^{(2)} = (2, 0)^T$  are the resting positions of the first and the second spring respectively. I estimated the time it takes for the particle to jump in the trap of the second spring, averaging upon  $N = 200$  realizations of the same system.

In other words, at  $T^* = 1$ ,  $\gamma = 1$  and  $K = 1$  I varied the initial location of the particle and then I computed the First Passage Time ( $FPT$ ) by looking at the instant the particle is closer to the second spring. The plotted  $FPTs$  are rescaled with respect to the simulation time step  $dt = 10^{-3}$ .

The initial positions chosen for the particle are:

$$\vec{r}(t_0) \in \{(0,0)^T, (0.125, 0.125)^T, (0.25, 0.25)^T, (0.5, 0.5)^T, (0.75, 0.75)^T, (1, 1)^T\}.$$

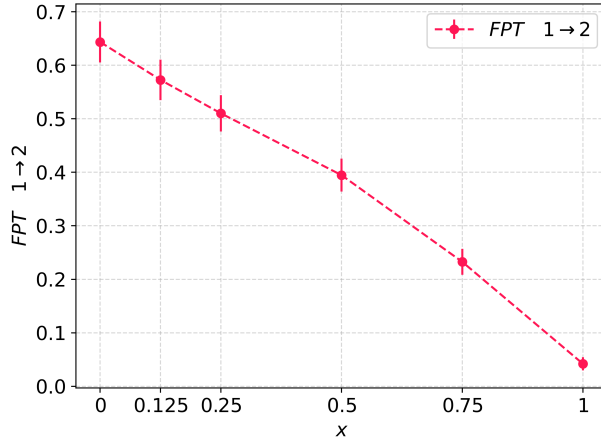


Figure 11.48: First Passage Time between the particle and the second probe position in the over-damped limit. Average over  $N = 200$  realizations

As expected, as the initial position is set closer to the second spring, the  $FPT$  decreases as well as its variance.

# 12 Reweighting techniques

## 12.18 Exercise: Change of measure

The one proposed is nothing than the importance sampling technique, with  $g$  a probability distribution function. Then, for a canonical distribution  $\pi$  at inverse temperature  $\beta$ , one can show that:

$$\begin{aligned}\langle O \rangle_\pi &= \frac{\sum_{i=1}^M O(\mathcal{C}_i) \pi(\mathcal{C}_i)}{\sum_{i=1}^M \pi(\mathcal{C}_i)} \\ &= \frac{\sum_{i=1}^M O(\mathcal{C}_i) \frac{\pi(\mathcal{C}_i)}{g(\mathcal{C}_i)} \cdot g(\mathcal{C}_i)}{\sum_{i=1}^M \frac{\pi(\mathcal{C}_i)}{g(\mathcal{C}_i)} \cdot g(\mathcal{C}_i)} \\ &= \left\langle O \frac{\pi}{g} \right\rangle_g \\ &\stackrel{(a)}{=} \frac{\langle O \frac{e^{-\beta E}}{g} \rangle_g}{\langle \frac{e^{-\beta E}}{g} \rangle_g}\end{aligned}$$

where  $M$  is the number of measurements and in (a) I introduced the canonical distribution  $\pi$  written as the Boltzmann target distribution.

## 12.19 Exercise: Single Histogram Method

Running  $K = 5$  simulations on the two-dimensional Ising model at temperatures

$$T_i \in \{0.5 \cdot T_c, 0.8 \cdot T_c, T_c, 1.5 \cdot T_c, 2 \cdot T_c\}$$

very far apart one from the other, the single histogram method has been applied, but with no significant results.

Indeed, sampling  $U(\beta)$  at these different temperatures, when trying to give an estimate of  $U(\beta')$  for  $\beta' \in \left( \frac{1}{\max(T_i)}, \frac{1}{\min(T_i)} \right)$  the results are unsatisfactory. The plot below on the *right* represents the attempt to estimate at temperatures  $T \neq T_i$ . One can see immediately that the output is meaningful only near the temperature considered. When one tries to reweight far from the examined  $T_k$ , results are far from the usual evaluation of the average internal energy per spin  $U(T_i) = \frac{\langle E(T_i) \rangle}{N}$ , here depicted as a red star (\*).

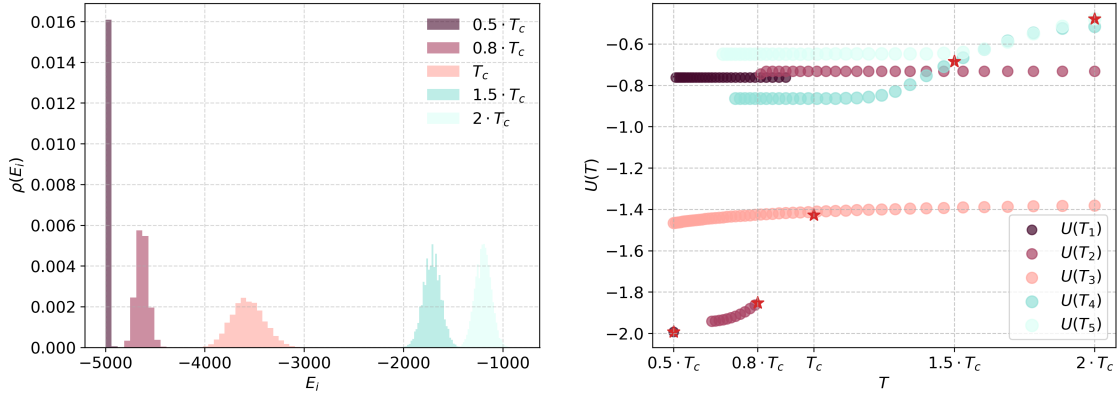


Figure 12.49: Absence of overlap: poor results from  $SHM - L = 50$

The *left* plot emphasizes the complete absence of overlaps between the energy distributions. In the *right* plot the average energy per spin  $U(T) = \frac{\langle E(T) \rangle}{N}$  is plotted, with  $N = L^2$  (here  $L = 50$ ). If one instead considers a more limited range of temperatures, such as

$$T_i \in \{T_c - 2\epsilon, T_c - \epsilon, T_c, T_c + \epsilon, T_c + 2\epsilon\}$$

where  $\epsilon = 10^{-2}$  for example, the plot below on the *left* illustrates the overlapping between the chains, and on the *right* a better application of the single histogram method.

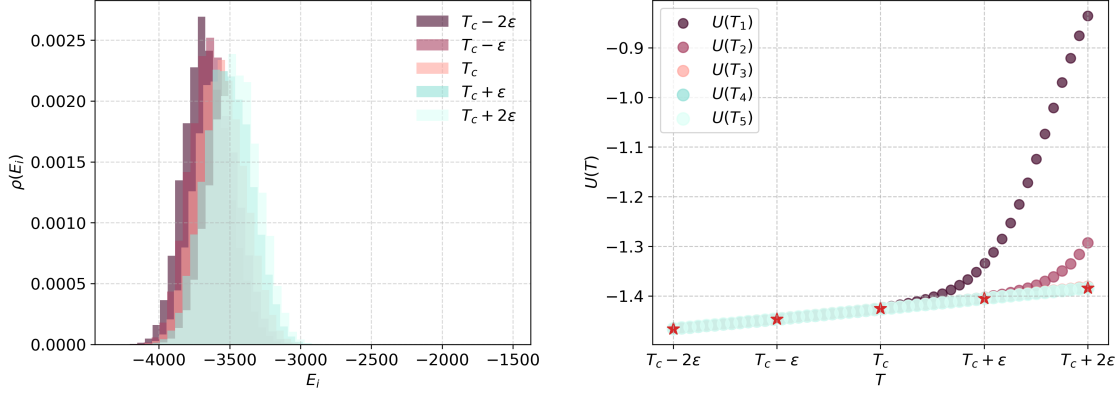


Figure 12.50: Overlap between chains: good results from  $SHM - L = 50$

Results are better but, especially for smaller temperatures - such as  $T_1$  and  $T_2$  - the extrapolated  $U(T_k)$  gets worse when far apart from  $T_i$ . This behaviour is not observed when one uses higher temperatures and reweights them to lower ones - see the lighter curves where the data set of the highest is reweighted to predict  $U(T_k)$ .

This peculiar behaviour could be explained considering the nature of the weights themselves. When passing from a lower to an higher temperature the exponent of Boltzmann weight will be negative, not allowing a good extrapolation of  $U(T_k)$ . This does not happen the other way around, when from higher temperatures one moves to lower ones. The contribution given by  $(\beta' - \beta)E_i$  will always be positive, allowing a better reweight.

## 12.20 Exercise: Multiple Histogram Method

Following the previous section, I estimated  $U(T)$  using the multiple histogram method.

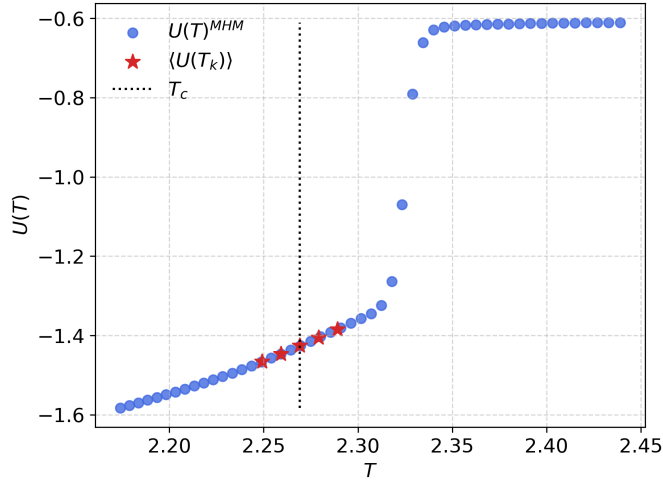


Figure 12.51: *MHM* predictions -  $L = 50$

The method works effectively allowing to have an estimate of different  $U(T_k)$  even outside the working range. There is very good agreement with the traditional evaluations of the average internal energy per spin  $U(T_i)$ , here depicted as red stars (\*).

The *MHM* has been used to compute the specific heat  $C(\beta)$  too. Following the same criterion developed to predict  $U(\beta)$ ,  $\langle U^2 \rangle_\beta$  has been estimated accordingly, and following

$$C(\beta) = \frac{N}{\beta^2} \left[ \langle U^2 \rangle_\beta - \langle U \rangle_\beta^2 \right]$$

the specific heat has been extrapolated<sup>(2)</sup> for three different system sizes:  $L \in \{20, 30, 50\}$ .

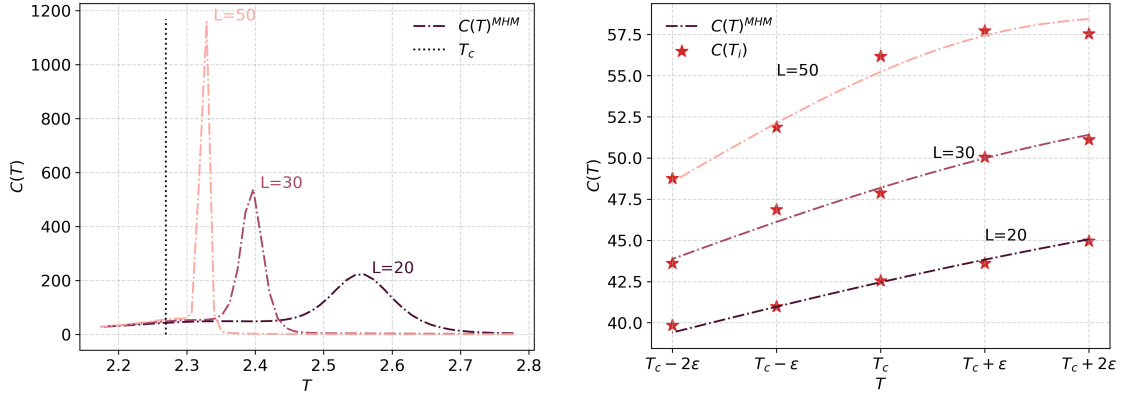


Figure 12.52:  $C(T)$  prediction on the *left* and closer look to usual evaluation of  $C(T_i)$  on the *right*

The *left* plot emphasizes the movement of  $C(T)$ 's maximum getting closer and closer to  $T_c$  as  $L$  increases, as one would expect. On the *right* instead the usual evaluation of  $C(T_i)$ , showing the estimates proposed by the multiple histogram method is in good agreement with those expected (\*).

Furthermore, I tried to rescale the measurements by the autocorrelation time  $\tau_i$  of stored data and the result I got is in good agreement with what already shown in previous plots.

<sup>(2)</sup>  $N$  appears at the numerator since the average energy per spin  $U(T) = \frac{\langle E(T) \rangle}{N}$  is considered.

# 13 Langevin simulation of many particles

## 13.21 Exercise: Cell list

Two implementations of the cell list algorithm have been performed in the provided code. The first one for *particle 0* and the second one for *smaller particles*. First, the *big particle* is placed in the middle of the box, while all the other particles are placed randomly in the cells created close to the center of *particle 0*.

Then, what changes is that the central particle experiences an harmonic force with respect to the resting position of a trap placed in the middle of the box and moving linearly with a velocity  $v_{trap}$ . All the *small particles* do not experience any kind of forces, exception made (even for the *big particle*) thermal fluctuations: the Langevin equation is considered for the whole system, therefore with movements characterized by random noise.

The *big particle* interacts then with all other particles with an exponential force, penalizing interactions between particles very far one from the other. The force applied satisfies the third law of dynamics, being of opposite sign for *particle 0* and for *small particles*.

*Small particles* then experience also a *small - small interaction*, characterized, even in this case, by a Gaussian repulsion term.

Moreover, when  $L_p > 1$  they experience a *polymer bonds interaction* too: here it can be found the piece of code I modified in order to accomplish the **Active Matter** implementation, using the  $N$  *small particles* as  $N/2$  **active dumbbells**. Therfore, I have introduces an harmonic force with the aim to keep apart particles  $i$  and  $i + 1$ , with resting length  $\Lambda = 1/2$ . Moreover, particles  $i$  and  $i + 1$  experience a propulsive force  $\vec{f}$  oriented as the vector  $\overrightarrow{r_i r_{i+1}}$ .

Removing the harmonic trap that keeps the probe confined and passing from "wrapped" to "unwrapped coordinates", I studied the diffusion of the probe in the bath of  $N/2$  active dumbbells.

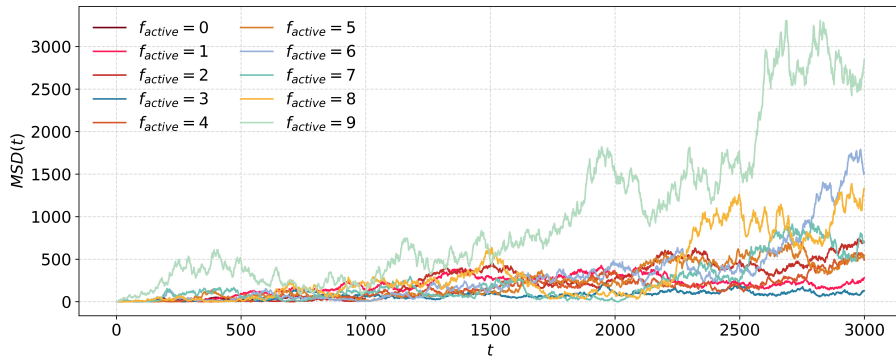


Figure 13.53: Mean Square Displacement (MSD) of the probe as a function of time  $t$  and  $f_{active}$

The above plot shows the Mean Square Displacement  $MSD(t)$  as a function of time and  $f_{active}$ ,

where<sup>(3)</sup>

$$f_{active} \in \{1, 2, 3, 4, 5, 6, 7, 8, 9\}.$$

The plot makes clear that as the value of  $f_{active}$  increases, the probe spreads out in space more rapidly. Higher fluctuations are due to the fact that only a single trajectory is considered for each value of  $f_{active}$ . One could perform many simulations and than plot the average of the different trajectories. The very same plot averaging on the *small particles* returns more defined lines, validating the expected linear trend.

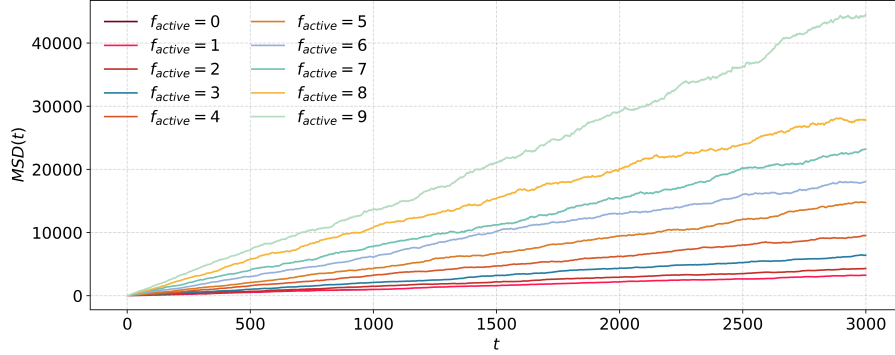


Figure 13.54: Mean Square Displacement (MSD) of the particles as a function of time  $t$  and  $f_{active}$ : average over  $N = 500$  particles

---

<sup>(3)</sup>All the provided input parameters can be found in the file *parameters.dat*.